

Please cite this article as: D. Yang, D. Laera, A.S. Morgans, A systematic study of nonlinear coupling of thermoacoustic modes in annular combustors, *Journal of Sound and Vibration* (2019), doi: <https://doi.org/10.1016/j.jsv.2019.04.025> ©2019. This manuscript version is made available under the CC-BY-NC-ND 4.0 license <http://creativecommons.org/licenses/by-nc-nd/4.0/>

## A systematic study of nonlinear coupling of thermoacoustic modes in annular combustors

Dong Yang<sup>a,\*</sup>, Davide Laera<sup>a</sup>, Aimee S. Morgans<sup>a</sup>

<sup>a</sup>*Department of Mechanical Engineering, Imperial College London, London, SW7 2AZ, UK*

---

### Abstract

Thermoacoustic instabilities in annular gas turbine combustors often involve modes which vary in both the longitudinal and circumferential directions. Recent experimental studies show that during limit cycle oscillations, different thermoacoustic modes may be uncoupled, as is the case in purely longitudinal or circumferential spinning modes. They may also be coupled, for example two counter-rotating circumferential modes combining to give standing or mixed modes, and coupling between circumferential and longitudinal modes giving rise to the slanted mode. Accurately predicting such modal couplings and the resulting spatial pattern of limit cycle oscillations remains an open challenge. This work uses a 2-D low-order network model based on modal expansions, validated against a full 3-D Helmholtz solver, to systematically investigate these couplings. For the first time, low-order network modelling is shown to capture limit cycle oscillations exhibiting both uncoupled and nonlinearly coupled modes, the latter including coupling between counter-rotating circumferential modes and between longitudinal and circumferential modes. It is shown that limit cycle solutions with totally different mode patterns (longitudinal, circumferential spinning, circumferential standing and slanted) can all exist in a given thermoacoustic system, with switches between modal patterns arising from slight changes in parameters such as the flame time delay.

**Keywords:** low-order network model, thermoacoustic instability, annular combustor, Helmholtz solver

---

### 1. Introduction

Due to stringent requirements on NO<sub>x</sub> emissions, modern aero-engines and ground-based gas turbines are often operated under lean combustion conditions. This makes combustion more susceptible to acoustic disturbances [1], with feedback between the acoustic and heat release perturbations then leading to a strong propensity to thermoacoustic instability, also known as combustion instability. Most investigations into combustion instability over recent decades have focused on single-burner configurations, where the combustors are long. However, many modern gas turbines utilise combustion systems which are annular in shape with many burners arranged around the annulus, this offering the advantages of short combustor size and more uniform exit temperatures. The circumference of such combustion systems is usually longer than or of the same order as the length, such that low frequency thermoacoustic modes can propagate in both the longitudinal and circumferential directions [2–4]. A variety of spatial patterns are then possible in the limit cycle oscillations which arise from instability. These include patterns [5–9] corresponding to: (i) purely longitudinal modes; (ii) circumferentially-varying modes which can be spinning, standing or some mixture of the two (and which may or may not sustain longitudinal variations, depending on the frequency and acoustic

---

\*Corresponding author

Email address: [d.yang13@imperial.ac.uk](mailto:d.yang13@imperial.ac.uk) (Dong Yang)

boundary conditions), and (iii) the newly identified slanted mode, so named as the distribution of heat release perturbations is slanted over the circumference. The ability to predict the spatial instability pattern in a given combustion system is important for designing out or controlling the instability [4, 10].

Prediction of thermoacoustic instabilities in annular combustors remains an ongoing challenge. Full compressible CFD simulations [11, 12] are possible, but are extremely computationally expensive. This is due to the range of length and time scales relevant to the key flow physics – the unsteady combustion, acoustic waves, turbulence and heat transfer – which makes them prohibitively expensive as a design tool. Computational approaches which couple separate treatments for the acoustics and the flame unsteadiness are more computationally efficient and provide a feasible alternative. They exploit the fact that in gas turbine combustors, the acoustic wave behaviour remains linear with respect to the mean flow, even during limit cycle oscillations. The flame is the main source of nonlinearity. Furthermore, in annular combustors which are “thin” i.e. whose annular gap is much smaller than their mean radius or axial length, the dependence on radius can be neglected [2]. This allows simplified computational, analytical or semi-analytical tools to be applied to the acoustic waves.

Recent work [13–19], has presented analytical modelling tools for annular combustors, focussing on acoustic wave propagation only in the circumferential direction. Longitudinal acoustic variations in both the plenum and the combustor, and axial mean flow effects are neglected. These tools have facilitated stability analysis of limit cycles with purely circumferential variations [16, 18], yielded insights into plenum-combustor coupling [13], the effect of burner differences and circumferential mean flow [14, 15], and flame response to circumferential perturbations [17, 19]. However, predictions and insights for more realistic annular combustors remain a challenge. The above tools cannot be used to analyse laboratory annular rigs, as these typically have acoustic boundary conditions which are close to those for a closed upstream end and open downstream end [6, 9]. Such closed-open boundary conditions always require longitudinal acoustic variations to be accounted for, even to simply predict the correct mode frequency. Furthermore, real industrial annular combustors often have axial lengths of the same order as their circumference, suggesting that co-existence and potential coupling between longitudinal and circumferential modes is likely to occur. Finally, the effect of mean flow on the acoustic propagation and damping, and perturbations in the form of convected entropy and vorticity waves may need to be properly accounted for.

For annular combustors, periodicity in the circumferential direction means that low frequency acoustic perturbations can be represented as the sum of a longitudinal propagating mode, and clockwise and anti-clockwise rotating circumferential modes with different circumferential wave numbers. That is, the Fourier amplitude of a given acoustic variable, can be represented as (e.g. for pressure)  $\tilde{p}(x, \theta, \omega) = \sum_{n=-N}^N \tilde{p}^{(n)}(x, \omega) e^{in\theta}$ , where  $\theta$  is the azimuth angle,  $x$  the axial location along the combustor,  $\omega$  the anular frequency and  $\tilde{p}^{(n)}$  the Fourier amplitude of circumferential mode  $n$  – with given numerical or experimental data, this can be obtained by using a space Fourier transform  $\tilde{p}^{(n)}(x, \omega) = 1/(2\pi) \int_0^{2\pi} \tilde{p}(x, \theta, \omega) e^{-in\theta} d\theta$ . If the combustor is axisymmetric throughout (in practice requiring a large number of identical, azimuthally equi-spaced flames) and perturbations remain within the linear regime, these modes behave completely independently and are uncoupled [20, 21]. Once the flame responses become nonlinear, the behaviour of different circumferential modes is no longer independent and they become coupled. Circumferential modes with opposite wavenumbers (for example,  $n = +1$  and  $n = -1$ ) can co-exist, combining to give circumferential standing modes if their amplitudes are the same, or mixed modes if their amplitudes differ. The “slanted mode” comprises the co-existence of both circumferential and longitudinal mode components [7]. Hence quite general modal couplings, not just between counter-rotating circumferential modes with opposite wave numbers, can occur, and predicting such couplings is key to the final spatial pattern exhibited in limit cycle oscillations.

Low-order network models built upon the idea of modal expansions deal naturally with co-existence of circumferential and longitudinal modes. They are founded on the convected wave equation, and account for physical effects such as mean flow and different acoustic boundary conditions. Such low-order network models were first developed for annular combustors around fifteen years ago, including by research groups at Cambridge university and TU Munich [2, 20–25]. Linear flame models have been used to study thermoacoustic mode stability [22] and asymmetry effect such as burner difference [24, 24]. Nonlinear flame models have also been used to study modes at limit cycles [20, 25]. However, they have not as yet been used for systematically predicting full oscillation behaviour – thermoacoustic limit cycle patterns dependent on the coupling between different circumferential modes, and between longitudinal and circumferential modes has not been systematically studied. Their ability to predict the frequency, amplitude and spatial pattern evolution between linearly unstable modes and limit cycles, and between different limit

cycles have also not as yet been systematically studied and validated.

In this paper, a two dimensional low-order network modelling framework (denoted by “LONM”) for annular combustors is presented, this following similar lines to [2, 21–26]. It is a frequency domain framework which accounts for both longitudinal and circumferential variations, modal couplings, mean flow effects and differing acoustic boundary conditions. The developed network tool is then applied to a laboratory annular combustor geometry from the EM2C lab [7, 9] with a given mean flow and a prescribed simple but generic nonlinear flame model. Depending on the parameters of the combustor model, a variety of limit cycle solutions are found, spanning purely longitudinal, circumferentially spinning, circumferentially standing and the more complicated “slanted mode” solutions. The predictions are analysed in detail, including the mode evolution with oscillation amplitude, the predicted limit cycle frequency, the predicted mix of mode strengths during limit cycle and the final axial and circumferential variation of the limit cycle mode shapes. These are all validated by comparison against predictions from a 3-D Helmholtz solver (denoted by “HS”) embedding the same geometry and nonlinear flame model. The power of the low-order network model in being able to accurately predict all of these limit cycle oscillation patterns is demonstrated. Both the low-order network modelling framework and the Helmholtz solver are frequency domain tools, and as such their prediction of the final limit cycle solution is dependent on the initial guess of the mix of mode contributions. The effect of this initial guess is finally studied, revealing how different limit cycle spatial patterns may be predicted for a given thermoacoustic system. A time domain framework would be needed to comment on the stability of predicted limit cycle solutions [16, 18, 20, 27]. Furthermore, the dependence of the final prediction on the flame model parameters is investigated, to reveal the strong sensitivity of especially the slanted mode to system parameters. Any secondary limit-cycles or non-constant limit-cycles are not considered by the present work and are left for future studies.

## 2. Low-order network model (LONM)

A typical annular combustor can be simplified to an annular-shaped plenum connected to an annular-shaped combustor by many premix ducts. The premix ducts are equi-spaced azimuthally and can be assumed cylindrical. Combustion occurs just downstream of interfaces between the premix ducts and the combustor, hence the premix ducts are also often termed “burners” [2, 13, 20, 23, 24, 26]. Both the plenum and the combustor can be represented as a narrow annular duct whose radial gap is much smaller than the axial and circumferential lengths, as shown in Fig. 1. At the low frequencies at which thermoacoustic instabilities tend to occur, high-order radial modes in the plenum and combustor are highly cut-off, meaning that only plane and circumferential waves can propagate. Furthermore, each burner can be assumed of small enough diameter that it can only sustain plane acoustic waves. Each burner inlet is exposed to oscillations from the plenum and each burner outlet is exposed to oscillations from the combustor, as shown in Fig. 2 (Top).

### 2.1. Governing equations and flow perturbations

#### 2.1.1. Governing equations

To build a model for analysing this system, we re-introduce ideas from [2, 21–26]. Firstly, we consider regions of the duct in which no combustion is occurring. By neglecting viscosity, heat input and heat conduction, assuming a steady uniform single-component mean flow and constant heat capacities, the Navier-Stokes equations governing fluid motion simplify to the following equations for linear perturbations [2]:

$$\left( \frac{1}{\bar{c}^2} \frac{\bar{D}^2}{Dt^2} - \nabla^2 \right) p' = 0, \quad (1a)$$

$$\bar{\rho} \bar{T} \frac{\bar{D}s'}{Dt} = 0, \quad (1b)$$

$$\frac{\bar{D}\xi'}{Dt} = \mathbf{0}, \quad (1c)$$

where  $\bar{D}/Dt = \partial/\partial t + \bar{\mathbf{u}} \cdot \nabla$ ,  $c$ ,  $\rho$ ,  $T$  are the sound speed, density and temperature respectively, and  $p$ ,  $s$ ,  $\bar{\mathbf{u}}$ ,  $\xi$  are pressure, entropy, velocity (with components  $(u, v, w)$ ) and vorticity respectively. An overbar,  $\bar{[ ]}$ , denotes time-average and a prime,  $[ ]'$ , denotes small perturbations.

Equation (1) shows that away from the combustion zone and for constant flow area, linear flow perturbations can be thought of as the sum of three types of disturbance, 1) an acoustic disturbance which is isentropic and irrotational, 2) an entropic disturbance that is incompressible and irrotational, and 3) a vortical disturbance that is incompressible and isentropic [2, 28].

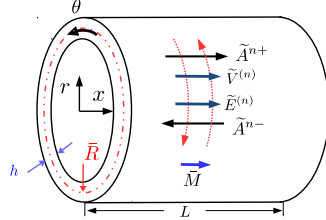


Figure 1: (Color online) A thin annular duct with a uniform low Mach number mean flow,  $\bar{M}$ . At low frequencies, high order radial modes are highly cut-off because  $h \ll 2\pi\bar{R}$  and  $h \ll L$ .  $n$  denotes circumferential wavenumber.  $\tilde{A}^{n\pm}$  are down- and upstream propagating acoustic waves,  $\tilde{V}^{(n)}$  is the vorticity wave, and  $\tilde{E}^{(n)}$  the entropy wave. Red dotted lines with arrows indicate that these waves may also propagate in the circumferential direction if  $n \neq 0$ .

### 2.1.2. Acoustic perturbations

Acoustic perturbations in a thin annular duct can be assumed to have only longitudinal and circumferential variations [2]. They can then be represented as an infinite expansion of modal solutions, truncated at mode number  $N$  to give:

$$p'_A(x, \theta, t) = \text{Re}[\tilde{p}_A(x, \theta)e^{-i\omega t}], \quad (2a)$$

$$\tilde{p}_A(x, \theta) = \sum_{n=-N}^N \tilde{p}_A^{(n)}(x, \theta). \quad (2b)$$

Each mode  $n$  represents a circumferential wavenumber, with  $n$  an integer to satisfy the circumferentially periodic boundary condition.  $\text{Re}[\cdot]$  denotes real part,  $\tilde{\cdot}$  denotes Fourier amplitude and  $[\cdot]_A$  denotes perturbations due to acoustic waves. Because Eq. (1a) is a convected wave equation,  $\tilde{p}_A^{(n)}$  will be comprised of separate downstream and upstream propagating components:

$$\tilde{p}_A^{(n)} = \tilde{A}^{n+} e^{in\theta+ik^{n+}x} + \tilde{A}^{n-} e^{in\theta+ik^{n-}x}, \quad (3)$$

with  $\tilde{A}^{n\pm}$  the amplitudes of the downstream and upstream propagating waves.  $k^{n\pm}$  are the axial wavenumbers given by

$$k^{n\pm} = \frac{-\bar{M}k \pm \sqrt{(k^2 - n^2(1 - \bar{M}^2)/\bar{R}^2)}}{1 - \bar{M}^2}, \quad (4)$$

where  $k = \omega/\bar{c}$ ,  $\bar{M} = \bar{u}/\bar{c}$  is the axial mean flow Mach number and  $\bar{R}$  the mean radius. The modal components of the acoustic density perturbation and the axial and circumferential acoustic velocity perturbations can be similarly written as follows, where  $\alpha^{n\pm} = -\omega + \bar{u}k^{n\pm}$ .

$$\tilde{p}_A^{(n)} = \frac{1}{\bar{c}^2} \tilde{A}^{n+} e^{in\theta+ik^{n+}x} + \frac{1}{\bar{c}^2} \tilde{A}^{n-} e^{in\theta+ik^{n-}x}, \quad (5a)$$

$$\tilde{u}_A^{(n)} = -\frac{k^{n+}}{\bar{\rho}\alpha^{n+}} \tilde{A}^{n+} e^{in\theta+ik^{n+}x} - \frac{k^{n-}}{\bar{\rho}\alpha^{n-}} \tilde{A}^{n-} e^{in\theta+ik^{n-}x}, \quad (5b)$$

$$\tilde{w}_A^{(n)} = -\frac{n}{\bar{R}\bar{\rho}\alpha^{n+}} \tilde{A}^{n+} e^{in\theta+ik^{n+}x} - \frac{n}{\bar{R}\bar{\rho}\alpha^{n-}} \tilde{A}^{n-} e^{in\theta+ik^{n-}x}. \quad (5c)$$

### 2.1.3. Entropy perturbations

Equation (1b) shows that entropy perturbations convect with the mean flow. They are furthermore incompressible and irrotational, such that they involve only density perturbations, with the  $n^{\text{th}}$  component of the modal representation being

$$\bar{\rho}_E^{(n)} = -\frac{1}{c^2} \bar{E}^{(n)} e^{in\theta+ik_0x}, \quad (6)$$

with  $\lceil \cdot \rceil_E$  denoting perturbations due to entropy,  $k_0 = \omega/\bar{u}$ ,  $\bar{E}^{(n)} = \bar{\rho}\bar{T}(\gamma-1)\bar{s}^{(n)}$  and  $\gamma$  the heat capacity ratio.  $\bar{P}_E^{(n)} = \bar{u}_E^{(n)} = \bar{w}_E^{(n)} = 0$ .

### 2.1.4. Vorticity perturbations

As two-dimensional flow perturbations exist, a vorticity disturbance in the radial direction may arise, with Eq. (1c) showing that it will also convect with the mean flow. The vorticity does not contribute to pressure or density oscillations: its relation to the velocity oscillations, can be written as  $\tilde{\xi} = (\partial\bar{w}_V/\partial x - \partial\bar{u}_V/\partial\theta/\bar{R})\mathbf{e}_r$ , where  $\mathbf{e}_r$  is a unit vector in the radial direction. By combining this with the mass conservation equation, the  $n^{\text{th}}$  component of the solution is

$$\bar{u}_V^{(n)} = \frac{n}{\bar{\rho}c} \bar{V}^{(n)} e^{ik_0x+in\theta}, \quad \bar{w}_V^{(n)} = -\frac{k_0\bar{R}}{\bar{\rho}c} \bar{V}^{(n)} e^{ik_0x+in\theta}, \quad (7)$$

where  $\bar{V}^{(n)} = i\bar{\rho}\bar{c}\bar{R} \cdot \tilde{\xi}^{(n)} / (n^2 + k_0^2\bar{R}^2)$ . where  $\lceil \cdot \rceil_V$  denotes perturbations due to vorticity waves and  $\bar{P}_V^{(n)} = \bar{\rho}_V^{(n)} = 0$ .

### 2.1.5. Relating the wave vector, flow vector and flux vector

The two acoustic waves, the entropy perturbation and the vorticity perturbation can be combined into a “wave vector”, defined as  $\mathbf{W}^{(n)}(x) = (\bar{A}^{(n)}, e^{ik_0x}, \bar{E}^{(n)}, e^{ik_0x}, \bar{V}^{(n)}, e^{ik_0x})^T$ . The pressure, density and velocity perturbations in Eqs. (3, 5, 6, 7) can be compactly embedded into a “flow vector”  $\mathbf{F}^{(n)}(x) = (\bar{P}^{(n)}, \bar{\rho}^{(n)}, \bar{u}^{(n)}, \bar{w}^{(n)})^T$ . When two different duct sections are connected, perturbations in the two ducts can be related by applying linearised flow conservation equations. Thus, mass flux,  $m = Spu$ , axial-momentum flux,  $f_{(x)} = Sp + mu$ , angular-momentum flux,  $f_{(\theta)} = Rmw$ , and energy flux,  $e = S\gamma pu/(\gamma-1) + m(u^2/2 + w^2/2)$ , where  $S$  denotes the cross-sectional area of the relevant duct, may need to be considered. It then becomes useful to define a “flux vector”  $\mathbf{J}^{(n)}(x) = (\bar{m}^{(n)}, \bar{f}_{(x)}^{(n)}, \bar{f}_{(\theta)}^{(n)}, \bar{e}^{(n)})^T$ . The relation between  $\mathbf{W}^{(n)}(x)$  and  $\mathbf{F}^{(n)}(x)$  can then be given by a wave-to-flow transfer matrix,  $\mathbf{F}^{(n)}(x) = \mathbf{M}_{\mathbf{WF}}^{(n)} \mathbf{W}^{(n)}(x)$ , and the relation between  $\mathbf{F}^{(n)}(x)$  and  $\mathbf{J}^{(n)}(x)$  by a flow-to-flux transfer matrix,  $\mathbf{J}^{(n)}(x) = \mathbf{M}_{\mathbf{FJ}}^{(n)} \mathbf{F}^{(n)}(x)$ , where  $\mathbf{M}_{\mathbf{WF}}^{(n)}$  and  $\mathbf{M}_{\mathbf{FJ}}^{(n)}$  are given in Appendix (A).

Wave propagation in the axial direction can be conveniently tracked using the above notation. For example, if the wave amplitudes at a reference location,  $x_0$ , are given, their values at  $x = x_0 + L$  can be obtained by  $\mathbf{W}^{(n)}(x_0 + L) = \mathbf{M}_{\mathbf{P}}^{(n)} \mathbf{W}^{(n)}(x_0)$ , where  $\mathbf{M}_{\mathbf{P}}^{(n)} = \text{diag}(e^{ik^{(n)}L}, e^{ik^{(n)}L}, e^{ik_0L}, e^{ik_0L})$ .

## 2.2. Relating perturbations in the plenum and combustor

Figure 2 (Top) shows a schematic diagram of an annular plenum (region 1) connected to an annular combustor (region 3) via  $D$  identical premix ducts (region 2) which are evenly distributed circumferentially. The central axis of the  $d^{\text{th}}$  premix duct is taken to have an azimuth angle of  $\Psi_d = 2\pi(d-1)/D$  radians. In general, the number of premix ducts is much larger than the highest circumferential wavenumber of thermoacoustic instabilities and so  $D \geq (2N+1)$ . Perturbations in both the plenum and combustor can be expressed in terms of the four waves outlined in Sec. 2.1, each written as an expansion of circumferential modes. It should be noted that when an annulus connects to a cylindrical duct, as occurs when the plenum/combustor meet the premix ducts in Fig. 2 (Middle), each cylindrical duct can only sustain the plane acoustic and entropy waves, with its vorticity always zero. We now derive the relations linking perturbations in the plenum and combustor.

### 2.2.1. From the plenum to the premix ducts

The mean flow from the plenum is assumed to divide equally between the premix ducts. For perturbations, the flux which passes into the  $d^{\text{th}}$  premix duct is assumed to originate from the annular sector of plenum extending just

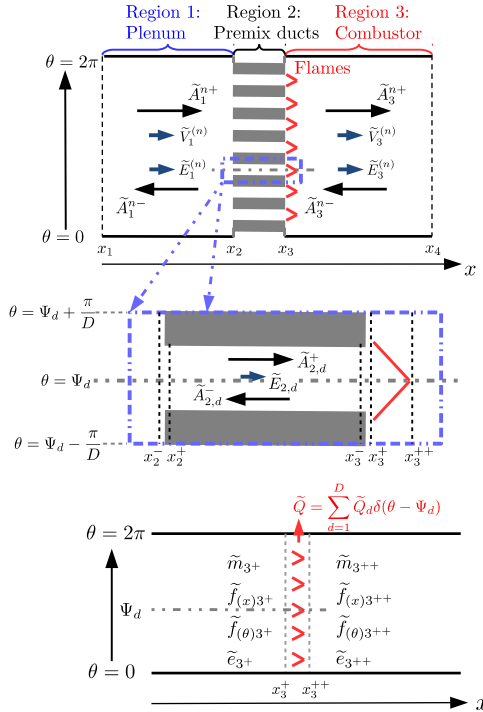


Figure 2: (Color online) (Top) A schematic diagram of an annular combustor comprising a plenum, combustor, and  $D$  premix ducts (burners) with flames at their outlets. (Middle) Details of one premix duct:  $x_2^-$  and  $x_2^+$  are the axial locations just before and after the duct inlet,  $x_3^-$  is the axial location just before the duct outlet,  $x_3^+$  just after the outlet but before the flame, and  $x_3^{++}$  just after the flame. (Bottom) Schematic of the  $D$  unsteady flames at the upstream end of the annular combustor, with the flux perturbations before and after the flames marked.

ahead of the premix duct, from  $\Psi_d - \pi/D < \theta < \Psi_d + \pi/D$ . Taking the mass flux perturbation at the inlet of the  $d^{\text{th}}$  premix duct as an example:

$$\tilde{m}_{2^+,d} = \int_{\Psi_d - \pi/D}^{\Psi_d + \pi/D} \sum_{n=-N}^N \frac{m_2^{(n)}}{S_1} e^{in\theta} \bar{R} h d\theta, \quad (8)$$

where  $S_1 = 2\pi\bar{R}h$  is the cross-sectional area of the plenum and subscripts  $[ ]_{2^-}$  and  $[ ]_{2^+}$  denote the axial locations just before and after the premix duct inlet, as shown in Fig. 2 (Middle). Energy flux perturbation can be similarly obtained. Because the flow contracts as it passes from the plenum into the premix ducts, it can be assumed isentropic [2]. Finally, the mass, entropy and energy flux conservations are written as

$$\tilde{m}_{2^+,d} = \frac{1}{D} \sum_{n=-N}^N \gamma^{(n)} \tilde{m}_2^{(n)} e^{in\Psi_d}, \quad (9a)$$

$$\tilde{s}_{2^+,d} = \frac{1}{D} \sum_{n=-N}^N \gamma^{(n)} \tilde{s}_2^{(n)} e^{in\Psi_d}, \quad (9b)$$

$$\tilde{e}_{2^+,d} = \frac{1}{D} \sum_{n=-N}^N \gamma^{(n)} \tilde{e}_2^{(n)} e^{in\Psi_d}, \quad (9c)$$

where  $\gamma^{(n)} = \sin(n\pi/D)D/(n\pi)$  if  $n \neq 0$  and equals 1 if  $n = 0$ .

Inside each of the premix ducts, perturbations contain only plane waves. The wave vector (two acoustic waves and one entropy wave) just after the  $d^{\text{th}}$  duct inlet, can then be obtained by multiplying the inverse of the wave-to-flux transfer matrix to the flux vector [2, 29, 30]

$$(\tilde{A}_{2^+,d}^+, \tilde{A}_{2^+,d}^-, \tilde{E}_{2^+,d})^T = [\mathbf{M}_{\text{F2J}}^{(p,2^+)} \mathbf{M}_{\text{W2F}}^{(p)}]^{-1} (\tilde{m}_{2^+,d}, \tilde{s}_{2^+,d}, \tilde{e}_{2^+,d})^T, \quad (10)$$

where  $\mathbf{M}_{\text{W2F}}^{(p)}$  and  $\mathbf{M}_{\text{F2J}}^{(p)}$  are now the wave-to-flow and flow-to-flux transfer matrices for plane waves respectively, given in Appendix (A)

The wave vector just before the outlet of the premix duct can be obtained by propagating the three plane waves from  $x_2^+$  to  $x_3^+$ ,

$$(\tilde{A}_{3^-,d}^+, \tilde{A}_{3^-,d}^-, \tilde{E}_{3^-,d})^T = \mathbf{M}_{\text{P}}^{(p)} (\tilde{A}_{2^+,d}^+, \tilde{A}_{2^+,d}^-, \tilde{E}_{2^+,d})^T, \quad (11)$$

where  $\mathbf{M}_{\text{P}}^{(p)} = \text{diag}(e^{ik^0 L_d}, e^{ik^0 L_d}, e^{ik_0 L_d})$  is the wave propagation matrix for plane waves, and  $L_d$  the length of the premix duct. Note that in the present paper, these matrices are the same for all the premix ducts as their geometry and mean flow parameters are assumed to be the same.

### 2.2.2. Between the premix ducts and the combustor

From the exit of each premix duct,  $x_3^+$ , to the start of the annular combustor with its larger flow area (but ahead of the flame),  $x_3^+$ , the conservation equations are applied. Mass and energy conservation are considered in a similar manner to section 2.2.1. Conservation of circumferential momentum requires  $\tilde{w}_{3^+}^{(n)} = 0$ . The flow expands across the premix duct exits, and the effect of the corresponding stagnation pressure loss on the perturbations can be accounted for by using the “separated flow” assumption that the static pressure immediately after the expansion matches that in the premix ducts ahead of the expansion [2, 31]. The axial momentum balance then gives  $\sum_{n=-N}^N \gamma^{(n)} \tilde{f}_{(x_3^+)}^{(n)} e^{in\Psi_d} = S_3 \tilde{p}_{3^-,d} + S_2 (\tilde{u}_2^2 \tilde{p}_{3^-,d} + 2\tilde{p}_2 \tilde{u}_2 \tilde{u}_{3^-,d}) = D \tilde{f}_{(x_3^-,d)}$ , where  $S_2$  is the overall cross-sectional area of the  $D$  ducts and  $S_3$  the cross-sectional area of the combustor. These mass, momentum and energy perturbations at the premix duct outlet can then be calculated from the corresponding wave vector by [2, 29, 30]

$$(\tilde{m}_{3^-,d}, \tilde{f}_{(x_3^-,d)}, \tilde{e}_{3^-,d})^T = \mathbf{M}_{\text{F2J}}^{(p,3^-)} \mathbf{M}_{\text{W2F}}^{(p)} (\tilde{A}_{3^-,d}^+, \tilde{A}_{3^-,d}^-, \tilde{E}_{3^-,d})^T, \quad (12)$$

where  $\mathbf{M}_{\text{F2J}}^{(p,3^-)}$  can also be found in Appendix (A).

Mass, momentum and energy equations are then written as

$$\frac{1}{D} \sum_{n=-N}^N \gamma^{(n)} \tilde{m}_3^{(n)} e^{in\Psi_d} = \tilde{m}_{3^-,d}, \quad (13a)$$

$$\frac{1}{D} \sum_{n=-N}^N \gamma^{(n)} \tilde{f}_{(x)3^+}^{(n)} e^{in\Psi_d} = \tilde{f}_{(x)3^-,d}, \quad (13b)$$

$$\frac{1}{D} \sum_{n=-N}^N \gamma^{(n)} \tilde{e}_{3^+}^{(n)} e^{in\Psi_d} = \tilde{e}_{3^-,d}. \quad (13c)$$

Combining Eqs. (9-13), we can obtain the relation between flux perturbations between just before the premix duct inlets and just after their outlets:

$$\begin{bmatrix} \sum_{n=-N}^N \gamma^{(n)} \tilde{m}_3^{(n)} e^{in\Psi_d} \\ \sum_{n=-N}^N \gamma^{(n)} \tilde{f}_{(x)3^+}^{(n)} e^{in\Psi_d} \\ \sum_{n=-N}^N \gamma^{(n)} \tilde{e}_{3^+}^{(n)} e^{in\Psi_d} \end{bmatrix} = \mathbf{M}_{\mathbf{F2J}}^{(p,3^-)} \mathbf{M}_{\mathbf{W2F}}^{(p)} \mathbf{M}_{\mathbf{P}}^{(p)} [\mathbf{M}_{\mathbf{F2J}}^{(p,2^+)} \mathbf{M}_{\mathbf{W2F}}^{(p)}]^{-1} \begin{bmatrix} \sum_{n=-N}^N \gamma^{(n)} \tilde{m}_2^{(n)} e^{in\Psi_d} \\ \sum_{n=-N}^N \gamma^{(n)} \tilde{s}_2^{(n)} e^{in\Psi_d} \\ \sum_{n=-N}^N \gamma^{(n)} \tilde{e}_2^{(n)} e^{in\Psi_d} \end{bmatrix} \quad (14)$$

where  $d = 1, 2, \dots, D$ . Because  $D \geq (2N + 1)$ , so the only solution for these equations is

$$\begin{bmatrix} \tilde{m}_{3^+}^{(n)} \\ \tilde{f}_{(x)3^+}^{(n)} \\ \tilde{e}_{3^+}^{(n)} \end{bmatrix} = \mathbf{M}_{\mathbf{F2J}}^{(p,3^-)} \mathbf{M}_{\mathbf{W2F}}^{(p)} [\mathbf{M}_{\mathbf{F2J}}^{(p,2^+)} \mathbf{M}_{\mathbf{W2F}}^{(p)}]^{-1} \begin{bmatrix} \tilde{m}_2^{(n)} \\ \tilde{s}_2^{(n)} \\ \tilde{e}_2^{(n)} \end{bmatrix}, \quad (15)$$

where  $-N \leq n \leq N$ . It can be seen that modes with different circumferential mode numbers,  $n$ , are not coupled with each other until now.

Across each individual flame, a flame model is prescribed. This relates the flame's normalised heat release rate fluctuation to the normalised axial velocity fluctuation at the outlet of each premix duct (i.e. at the  $x_3^-$  location). A general frequency domain description of the weakly nonlinear flame model,  $\mathcal{T}^{(d)}(\omega, |\tilde{u}_d|)$ , is

$$\frac{\tilde{Q}_d}{\bar{Q}_d} = \mathcal{T}^{(d)}(\omega, |\tilde{u}_d|) \frac{\tilde{u}_d}{\bar{u}_d}, \quad (16)$$

where  $\tilde{Q}_d$  and  $\bar{Q}_d$  are the fluctuating and mean heat releases from the  $d^{\text{th}}$  flame, and  $\tilde{u}_d$  and  $\bar{u}_d$  are the fluctuating and mean axial velocities at the outlet of the  $d^{\text{th}}$  premix duct. The flame model is nonlinear if it accounts for frequency and velocity amplitude dependence, and linear if it only exhibits frequency dependence. Note that it is possible to prescribe different flame models for different flames, although the same model is used across all flames in this paper. Transverse motion of the flame [32] is also neglected.

As shown in Fig. 2 (Bottom), with the heat release rate from each flame given by the flame model, the perturbations before  $(x_{3+})$  and after  $(x_{3++})$  the flames are deduced by assuming that the flame zone is axially compact (i.e. short compared to the acoustic wavelengths). Then, quasi-steady flow conservation jump equations are be applied across the flame zone axially. Azimuthally, the flames can be assumed to act as Dirac delta functions at azimuth angles  $\Psi_d$ , such that  $\tilde{Q}(\theta) = \sum_{d=1}^D 2\pi \tilde{Q}_d \delta(\theta - \Psi_d)$ . The expressions for the mass, momentum and energy conservation across the

flame are then

$$\sum_{n=-N}^N \tilde{m}_{3^+}^{(n)} e^{in\theta} = \sum_{n=-N}^N \tilde{m}_{3^+}^{(n)} e^{in\theta}, \quad (17a)$$

$$\sum_{n=-N}^N \tilde{f}_{(x)3^+}^{(n)} e^{in\theta} = \sum_{n=-N}^N \tilde{f}_{(x)3^+}^{(n)} e^{in\theta}, \quad (17b)$$

$$\sum_{n=-N}^N \tilde{f}_{(\theta)3^+}^{(n)} e^{in\theta} = \sum_{n=-N}^N \tilde{f}_{(\theta)3^+}^{(n)} e^{in\theta}, \quad (17c)$$

$$\sum_{n=-N}^N \tilde{e}_{3^+}^{(n)} e^{in\theta} + \sum_{d=1}^D 2\pi \tilde{Q}_d \delta(\theta - \Psi_d) = \sum_{n=-N}^N \tilde{e}_{3^+}^{(n)} e^{in\theta}, \quad (17d)$$

By multiplying  $e^{-in'\theta}$ , where  $-N \leq n' \leq N$ , on both sides of Eqs. (17) and integrating from  $\theta = 0$  to  $2\pi$ , these simplify to

$$\tilde{m}_{3^+}^{(n')} = \tilde{m}_{3^+}^{(n')}, \quad \tilde{f}_{(x)3^+}^{(n')} = \tilde{f}_{(x)3^+}^{(n')}, \quad \tilde{f}_{(\theta)3^+}^{(n')} = \tilde{f}_{(\theta)3^+}^{(n')}, \quad \tilde{e}_{3^+}^{(n')} + \sum_{d=1}^D \tilde{Q}_d e^{-in'\Psi_d} = \tilde{e}_{3^+}^{(n')}. \quad (18)$$

Because the flame models are applied at each separate flame, they are dependent on the axial velocity at a point (which will have contributions from many circumferential modes) rather than a modal component. If the flame models are linear, linear summation will mean that circumferential modes remain uncoupled. However, if they are nonlinear, they will then result in nonlinear coupling between circumferential modes. Note that  $n'$  is a dummy integration variable, which is replaced by  $n$  again henceforth.

### 2.2.3. Boundary conditions and the eigenvalue system

At the boundaries of the system – the plenum inlet and the combustor outlet – generic acoustic boundary conditions can be incorporated. For example, if  $R_{(A)1}^{(n)}$ ,  $R_{(E)1}^{(n)}$  and  $R_{(V)1}^{(n)}$  are respectively the inlet acoustic, entropy and vorticity reflection coefficients to an incoming (upstream propagating) acoustic wave with circumferential wavenumber  $n$  [33], the wave vector  $\mathbf{W}^{(n)}(x_1)$  at the plenum inlet can be written as

$$(\tilde{A}_1^{(n)}, \tilde{A}_1^{(n)}, \tilde{E}_1^{(n)}, \tilde{V}_1^{(n)})^T = \lambda^{(n)} (R_{(A)1}^{(n)}, 1, R_{(E)1}^{(n)}, R_{(V)1}^{(n)})^T, \quad (19)$$

where  $\lambda^{(n)}$  is the upstream-travelling strength of the  $n^{\text{th}}$  modal component.

Similarly for the combustor outlet, if the outlet acoustic reflection coefficients corresponding to a unit incoming (downstream-travelling) acoustic, entropy and vorticity wave with circumferential wavenumber  $n$  [33] are  $R_{(A)4}^{(n)}$ ,  $R_{(E)4}^{(n)}$  and  $R_{(V)4}^{(n)}$  respectively, the boundary conditions can be written as

$$R_{(A)4}^{(n)} \tilde{A}_4^{n+} + R_{(E)4}^{(n)} \tilde{E}_4^{(n)} + R_{(V)4}^{(n)} \tilde{V}_4^{(n)} - \tilde{A}_4^{n-} = 0. \quad (20)$$

To build the thermoacoustic system, we need to link perturbations at the system inlet to that at the outlet. We know that modal components with different  $n$ s are not coupled when they are propagating in the sections both before and after the flames, but are coupled across the flames. So the relation between perturbations at the system inlet and outlet can be obtained by propagating different components from the inlet to the premix duct outlets where they are summed up to calculate the flame heat release perturbations, applying conservation equations across the flames to obtain perturbations after the flames, decomposing perturbations after the flames into different modes and propagating them to the system outlet.

The linear propagation and flux conservation operations are firstly used to link the flow perturbations at the outlet of the premix ducts, ahead of the expansion into the combustor (i.e. the  $x_3$  location), to the modal component strengths at the plenum inlet. This accounts for propagation/convection along the plenum, interfacing to the premix ducts and propagation/convection along the premix ducts, and gives

$$(\tilde{p}, \tilde{\rho}, \tilde{u}, \tilde{w})_{3^-.d}^T = \mathbf{M}_{w2p}^{(0)} (\lambda^{(-N)} \dots \lambda^{(0)} \dots \lambda^{(N)})^T, \quad (21)$$

where  $d = 1, 2, \dots, D$ ,  $\mathbf{M}_{\omega 2p}^{(d)}$  is a  $4 \times (2N + 1)$  matrix which links the perturbations at the plenum inlet and the premix duct outlet and it is a function of only the angular frequency, system geometry, mean flow and thermodynamic parameters.

The axial velocity perturbation can be extracted from Eq. (21) and fed into the flame model of Eq. (16), in order to calculate the unsteady heat release rate from each flame. The jump relations across the flames, Eqs. (18), then give modal flux amplitudes after the flames (from which wave and flow perturbations can be deduced), and the propagation operator then gives the perturbations at the combustor outlet, where the outlet boundary conditions are applied.

By combining Eqs. (16) and (18) to (21) and considering all modes, the final eigenvalue system is then written as

$$\mathbf{M}_{120}(\omega, \lambda)\lambda = \mathbf{0}, \quad (22)$$

where  $\lambda = (\lambda^{(-N)} \dots \lambda^{(0)} \dots \lambda^{(N)})^T$  is the modal strength vector and  $\mathbf{M}_{120}$  is a  $(2N + 1) \times (2N + 1)$  matrix which embeds the perturbation relations between the inlet and outlet and satisfies both boundary conditions.

If the flame model is linear,  $\mathbf{M}_{120}$  does not depend on  $\lambda$ , which means  $\mathbf{M}_{120}(\omega)\lambda = \mathbf{0}$  – solving  $\det(\mathbf{M}_{120}(\omega)) = 0$  gives the frequencies and growth rates of the thermoacoustic modes. However, the full nonlinear system  $\mathbf{M}_{120}(\omega, \lambda)\lambda = \mathbf{0}$  needs to be solved if nonlinear flame models are considered. This is because the flame model would be nonlinearly dependent on velocity amplitude at premix duct outlets, these depending on the strengths of different modal components.

#### 2.2.4. Solution of the eigenvalue system

For a given system geometry, mean flow, thermodynamic parameters, boundary conditions and flame models, the eigenvalue problem in Eq. (22) can be solved numerically to obtain the eigenvalues (giving the frequency  $f$  and growth rate  $G_r$  of the thermoacoustic modes) and eigenvectors (giving their mode shape or spacial pattern). This is very efficient because the circumferential wavenumber of interest is usually very small (e.g.  $n = 0, \pm 1$ ), and taking  $N = 3$  is generally large enough for convergence in most cases, as shown in Appendix (B). Thus only  $(2N + 1)$  equations need to be solved in order to resolve this eigenvalue system.

If a linear flame model is used, the only unknown in  $\mathbf{M}_{120}$  is the complex angular frequency,  $\omega = 2\pi f + iG_r$ . The complex angular frequency can then be calculated by solving for the determinant of  $\mathbf{M}_{120}$  being zero. When a nonlinear flame model is used,  $\mathbf{M}_{120}$  is a function of both  $\omega$  and  $\lambda$ . One way to obtain limit cycle solutions is to enforce zero growth rate and search for frequencies and corresponding  $\lambda$ s which satisfy Eq. (22). Another way is to start with the linear flame model corresponding to the nonlinear model with a very small perturbation amplitude. This is used to find the mode of interest (which is usually unstable). Then a solution with the nonlinear flame model is sought by slightly reducing the growth rate and using an initial guess which has the frequency and modal amplitudes matching those for the linear case: the solution is likely to have a yet smaller growth rate and slightly increased modal amplitudes. This procedure is repeated until the growth rate goes to zero, yielding a limit cycle solution.

### 3. Test cases

The low-order network modelling tool is applied to test cases whose geometry matches that of the MICCA combustor from the EM2C lab [7, 9, 34]. This consists of a thin annular plenum connected by 16 burners (or premix ducts) to a thin annular combustor of the same mean radius, as shown in Fig. 4. The mean plenum/combustor radius is  $\bar{R} = 0.175$  m, the plenum has length 0.07 m and cross-sectional area  $0.077 \text{ m}^2$  and the combustor has physical length 0.2 m augmented of 41 mm to account for an outlet end correction [34, 35] and cross-sectional area  $0.055 \text{ m}^2$ . Each of the burners consists of two sections, an upstream section of length 0.014 m and cross-sectional area  $8.75 \times 10^{-4} \text{ m}^2$ , corresponding to the bottom part of the matrix burners, and a downstream section of length 0.006 m and cross-sectional area  $2.8 \times 10^{-4} \text{ m}^2$ , corresponding to the length and total cross-sectional area of the small holes of the matrix burners. To account for plane acoustic wave scattering near cross-sectional area changes, 5 mm and 3 mm correction lengths are added to the bottom and hole part of each burner respectively [36]. The mean pressure, temperature, velocity at the inlet are  $10^5 \text{ Pa}$ ,  $300 \text{ K}$  and  $0.094 \text{ m/s}$  respectively, and the mean temperature after the flame is  $1500 \text{ K}$ . The plenum inlet is taken to be an acoustically closed boundary condition, and the combustor outlet acoustically open. Note that acoustic energy loss at either end can be conveniently taken into account for a real combustor provided a

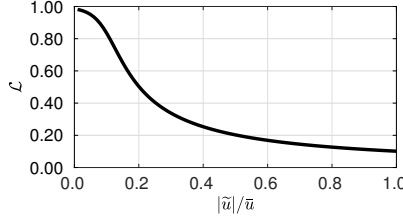


Figure 3: The amplitude function,  $\mathcal{L}$ , for the nonlinear flame model.

proper acoustic boundary condition [37], but they are assumed to be negligible in the current study, so the acoustic damping mainly comes from the acoustic flow interactions at the cross-sectional area changes.

Both linear and nonlinear flame models are considered. The linear model is a simple  $n - \tau$  model,  $\mathcal{T}^L(\omega) = n_f^L e^{i\omega\tau_f^L}$  with  $n_f^L = 1$  and  $\tau_f^L = 1$  ms. The nonlinear model has the form [29],

$$\mathcal{T}^N(\omega, |\tilde{u}/\bar{u}|) = \mathcal{L} n_f^L e^{i\omega(\tau_f^L + \tau_f^N(1-\mathcal{L}))}, \quad (23)$$

where  $\mathcal{L}$  is a function of  $|\tilde{u}/\bar{u}|$  with the relation

$$\mathcal{L}(|\tilde{u}/\bar{u}|) \left| \frac{\tilde{u}}{\bar{u}} \right| = \int_0^{|\tilde{u}/\bar{u}|} \frac{1}{1+(x+\alpha)^\beta} dx. \quad (24)$$

$\tau_f^N = 0.1$  ms,  $\alpha = 0.9$  and  $\beta = 40$  are used, with the corresponding shape of  $\mathcal{L}$  shown in Fig. 3. Note that this nonlinear flame model expression was presented in [29] along with validation against experimental data. It offers a more physically representative smooth saturation, unlike the abrupt saturation in [20, 38]. It also allows the flame model to be prescribed in terms of velocity fluctuation input, which is more physical and more widely used than the pressure fluctuation input used in [16]. Real flame response data could instead be incorporated if provided numerically or experimentally. We have chosen flame model parameters to be within the range of physically observed values, specifically choosing certain values which exhibit mode switching.

#### 4. Helmholtz Solver (HS) and modal decomposition

To validate predictions from the low-order network modelling framework, the full three-dimensional geometry of the MICCA combustor, as shown in Fig. 4, is analysed by combining a Helmholtz solver framework with the above mentioned flame models. The methodology follows the procedure outlined in [34]: 16 flames located at the burner outlets along with a linear acoustic damping coefficient,  $\varepsilon$ , are incorporated into the Helmholtz equation to give

$$\frac{\omega^2}{c^2} \tilde{p} + i \frac{4\pi\omega\varepsilon}{c^2} \tilde{p} + \tilde{\rho} \nabla \cdot \left( \frac{1}{\tilde{\rho}} \nabla \tilde{p} \right) = i\omega \frac{\gamma-1}{c^2} \tilde{q}. \quad (25)$$

The flame response modelling follows [34] in using a weakly nonlinear approach to couple Eq. (25) with the nonlinear flame model of Eq. (23), treating the nonlinear problem as a perturbation of a linear problem. For each flame, Eq. (23) is linearised by fixing the velocity fluctuations level  $|\tilde{u}/\bar{u}|$ . Starting from the linear regime, the velocity fluctuation amplitude is increased until a limit cycle condition is reached. For each flame amplitude level,  $|\tilde{u}/\bar{u}|_j$ , the azimuthal distribution of  $|\tilde{u}/\bar{u}|$  is determined from the velocity eigenmodes computed by the code as:

$$|\tilde{u}/\bar{u}|(\theta) = \psi(\theta) |\tilde{u}/\bar{u}|_{max}, \quad (26)$$

where  $\psi(\theta)$  is the normalised velocity eigenmode. In contrast to [34], the analysed mode is not selected *a priori*, with  $\psi$  left free to change during the calculation depending on the modal frequency and pattern. An initial velocity

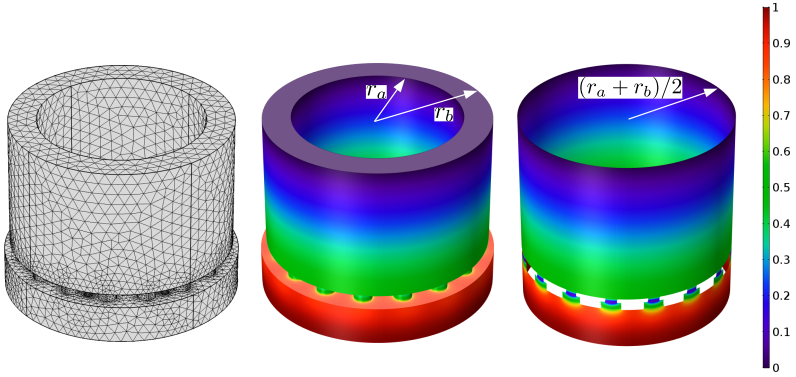


Figure 4: (Color online) (Left) The 3-D Helmholtz solver mesh (image adapted from [35]). (Middle) A 3-D mode shape in pressure for a longitudinal mode. (Right) A 2-D mode shape in pressure showing the same longitudinal mode.

perturbation pattern,  $\psi_0$ , is prescribed in order to faster reach convergence, but this does not affect the accuracy of the final converged mode solution.

Unlike the Helmholtz solver framework which neglects convective effects, the low-order network modelling framework includes them and so its modelling assumptions inherently account for the dissipation of acoustic energy due to mean flow effects, such as vortex shedding at mean flow expansions. The dependence of such dissipation on the frequency and mode shape is also naturally built in. On the contrary, the Helmholtz solver calculation requires the damping,  $\varepsilon$ , to be prescribed as an input parameter: it can differ depending on mode and is obtained by tuning to match the mode growth rate at one oscillation amplitude (such as matching the mode growth rate with the linear flame model), and then fixed during tracking of the mode evolution.

For a resolved thermoacoustic mode, the Helmholtz solver yields a 3-D pressure mode shape, such as that shown in Fig. 4 (middle). The corresponding 2-D mode shape (Fig. 4 (right) and Fig. 5 (Top)) can be extracted by averaging over the narrow gap between  $[r_a, r_b]$  for each  $(x, \theta)$  location. Then, a space Fourier transform over the circumference at each given axial location,  $x$ , (e.g. over the black dash line shown in Fig. 5 (top)) is used to decompose this pressure mode shape into different circumferential components:

$$\tilde{p}^{(n)}(x) = \frac{1}{2\pi} \int_{\theta=0}^{2\pi} \tilde{p}(x, \theta) e^{-in\theta} d\theta, \quad (27)$$

where  $n = 0, \pm 1, \pm 2, \dots$ . The  $n = 0$  and the combination of the  $n = \pm 1$  components are shown in Fig. 5 (bottom). A mode for which the longitudinal component ( $n = 0$ ) dominates is shown in Fig. 5 as an example.

## 5. Thermoacoustic mode predictions

### 5.1. The linear flame model case

For the MICCA combustor geometry with the linear flame model, the predicted thermoacoustic modes below 600 Hz include two unstable modes: (517 Hz,  $567 \text{ s}^{-1}$ ) and (557 Hz,  $352 \text{ s}^{-1}$ ). The first is a purely longitudinal mode with only the  $n = 0$  component non-zero in the modal amplitude vector,  $\lambda$ . The second is more complicated. Firstly, either or both of the  $n = \pm 1$  components can be non-zero in  $\lambda$  (scales are arbitrary due to linearity). This is because the  $n = \pm 1$  components are now degenerate (uncoupled) so each of them can exist independently [13, 15, 16, 18] and the mode shape in the circumferential direction is undetermined – it can be spinning, standing, or mixed. Secondly, this mode propagates both longitudinally and circumferentially.

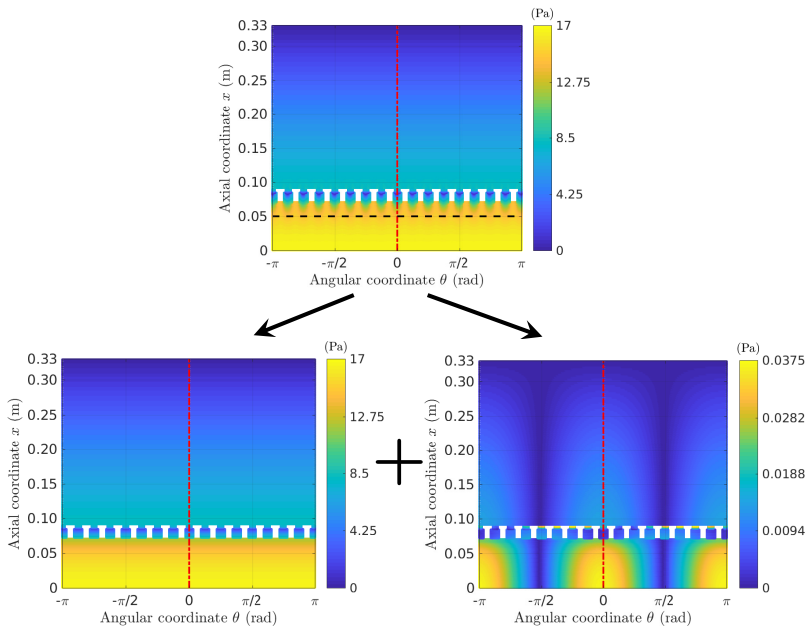


Figure 5: (Color online) Helmholtz solver results for (Top) the original pressure mode shape,  $|\tilde{p}(x, \theta)|$ , of a longitudinal mode with (bottom left) its purely longitudinal component,  $|\tilde{p}^{(0)}(x)|$ , and (bottom right) the combination of its  $n = \pm 1$  circumferential components,  $|\tilde{p}^{(1)}(x)e^{i\theta} + \tilde{p}^{(-1)}(x)e^{-i\theta}|$ .

### 5.2. Non-linear flame model: longitudinal mode

The MICCA combustor geometry with the nonlinear flame model of Eqs. (23) and (24) is now considered. We start by solving for the unstable longitudinal mode, (517 Hz,  $567 \text{ s}^{-1}$ ). This is done by enforcing the growth rate in  $\omega$  to be  $G_r^{(1)} = 560 \text{ s}^{-1}$  (slightly lower than for the linear mode), solving Eq. (22) with an initial frequency guess,  $f^{(0)}$ , close to 517 Hz and a small amplitude initial wave strength guess,  $\lambda^{(0)}$ , close to that for a longitudinal mode (with  $\lambda^{(0)}$  much larger than the other components). The resolved frequency and mode strengths,  $[f^{(1)}, \lambda^{(1)}]$ , are shown on the far right of Fig. 6 – they are very close to those for the linearly unstable longitudinal mode. The enforced growth rate  $G_r^{(2)} = G_r^{(1)} - \epsilon$  is then slightly reduced further, with  $[f^{(1)}, \lambda^{(1)}]$  the new initial guess, yielding  $[f^{(2)}, \lambda^{(2)}]$ , such that a longitudinal mode with a slightly larger wave amplitude and lower growth rate is found. This is repeated until a zero growth rate (limit cycle) solution is obtained.

Fig. 6 shows the predicted mode evolutions, with both the frequency and growth rates predicted by the low-order network modelling framework agreeing very well with those from the Helmholtz solver. The evolution of the mode strengths, including the dominant  $n = 0$  and the zero  $|n| > 1$  components, also agree well with the Helmholtz solver results, with the small strength difference in  $\lambda^{(0)}$  near the limit cycle most probably arising from a small acoustic damping rate difference. This confirms that the low-order network model can capture the frequency evolution and mode strength of the longitudinal mode.

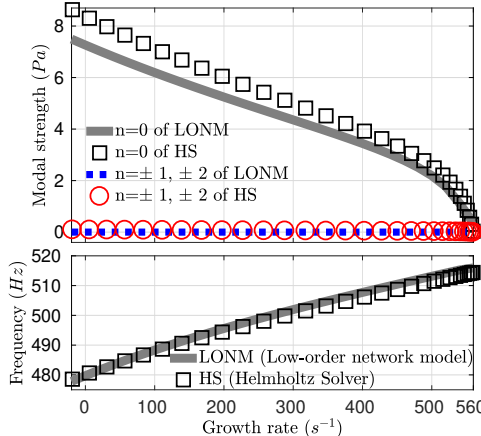


Figure 6: (Color online) Evolution of the longitudinal mode. (Top) the strength of different modal components in  $\lambda$  at the plenum inlet. (Bottom) the mode frequency.  $N = 3$  is used in the low-order network model, but only  $|n| \leq 2$  is plotted for the strengths. The Helmholtz solver results are obtained with  $\epsilon = 30 \text{ s}^{-1}$ .

The axial variation of this mode shape during the limit cycle is plotted in Fig. 7. The closed-open boundary condition is clearly seen to be satisfied. Both the amplitude and phase of the longitudinal component of the Helmholtz solver results overlap almost perfectly with those from the full Helmholtz solver (across all modal components). This confirms that the mode is a longitudinal mode, with evanescent (cut-off) higher order circumferential modes induced near cross-sectional area changes but rapidly decaying with distance. Both the amplitude and phase of the mode shape predicted by the low-order network model agree well with the Helmholtz solver, confirming that the low-order network model predicts the correct mode shape of the purely longitudinal mode.

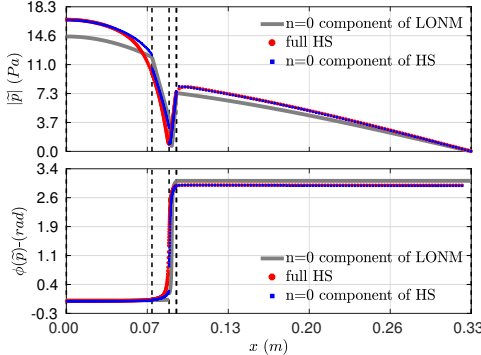


Figure 7: (Color online) Axial pressure mode shape of the longitudinal limit cycle – (Top) the amplitude and (bottom) the phase.  $\theta = 0$  (shown by the red dash line in Fig. 5) is considered. Only the  $n = 0$  component is plotted in the low-order network model. Vertical dashed black lines denote the cross-sectional area changes.

### 5.3. Non-linear flame model: spinning/standing mode

With the nonlinear flame mode, the evolution of the second linearly unstable mode, (557 Hz,  $352 \text{ s}^{-1}$ ) can also be investigated. The main difference compared to the purely longitudinal mode is that the final spatial pattern depends on the initial guess of the modal amplitudes. If the initial guess is close to a spinning mode (with either  $\lambda^{(1)}$  or  $\lambda^{(-1)}$  much larger than all the other components), the solution will be a spinning mode, but if the initial guess is close to a standing mode (with  $\lambda^{(1)}$  the same order of magnitude as each other and much larger than all other components), it will be a standing mode. At very small amplitudes, both the spinning and standing modes tend to the linearly unstable mode, as can be seen on the far right of Fig. 8 (Left and Right). As the amplitudes increase, both modes are gradually stabilized towards limit cycles. For both modes, the low-order network model predictions agree very well with the Helmholtz solver for both the evolution of the frequencies and the modal strengths.

The axial variation of the pressure mode shape in the spinning limit cycle is shown in Fig. 9a. The closed-open boundary condition is again satisfied. The spinning component clearly dominates the pressure mode shape for the Helmholtz solver results, confirming that this is a spinning mode. The agreement between the low-order network model and the Helmholtz solver is good. The predicted phase difference between the plenum and the combustor is about  $0.75 \text{ rad}$ , this corresponding to the nodal-line shift between the plenum and combustor studied by [39]. The value of this shift agrees with the  $\approx 0.73 \text{ rad}$  result given by the instantaneous pressure snapshot of the  $n = 1$  modal component from the Helmholtz solver, as shown in Fig. 9b. All of the above confirms that the low-order network model is able to accurately predict spinning limit cycles which propagate both circumferentially and longitudinally.

An important difference between spinning and standing circumferential modes is the azimuthal variation of the velocity perturbation amplitudes seen by the flame models. For a spinning mode, the same perturbation amplitude is seen over all 16 burner outlets, and hence flame models. However, for a standing mode, the standing mode pattern means that different flame models see different velocity amplitudes. The standing mode pattern predicted for the present standing mode is shown in Fig. 10b. It exhibits pressure and velocity nodes at the 5<sup>th</sup> and 13<sup>th</sup> burners, and amplitude anti-nodes at the 1<sup>st</sup> and 9<sup>th</sup> burners are seen. These predictions agree across the low-order network model and Helmholtz solvers. Note that this node/anti-node distribution is not the only solution for the standing limit cycle (the solution number depends on the burner numbers [18]) – with different initial guesses for  $\lambda$ , solutions with different distributions can be found.

The axial variation of the mode shape is shown in Fig. 10a, confirming general agreement between the low-order network model and the Helmholtz solver. As discussed in detail in Appendix (B), compared to the longitudinal and

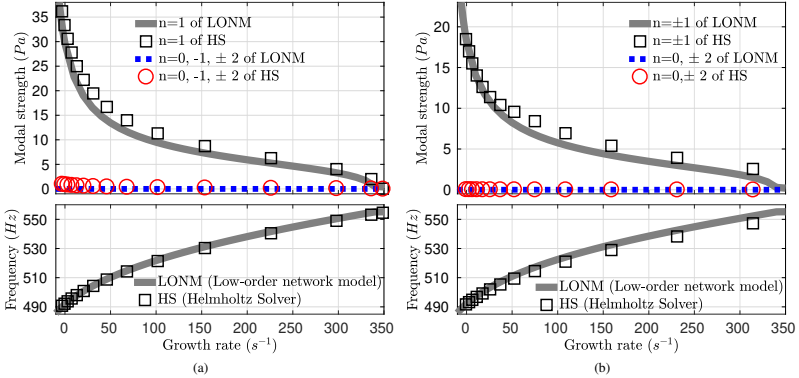


Figure 8: (Color online) Evolution of the (a) spinning mode and (b) standing mode. (Top) the strength of different modal components in  $\lambda$  at the plenum inlet and (Bottom) the mode frequency.  $N = 5$  is used in the low-order network model, but only  $|n| \leq 2$  is plotted for the strengths. The Helmholtz solver results are obtained with  $\varepsilon = 9 \text{ s}^{-1}$ .

spinning modes, a slightly larger phase difference between the original Helmholtz solver results and its “1st standing” modal component is seen after the burner outlets. This is because the nonlinear flame response couples the dominant  $n = \pm 1$  components with higher order modal components ( $n = \pm 3, \pm 5...$  in the present case), resulting in more noticeable higher order evanescent contributions near the burners – these decay exponentially away from the burners and do not significantly change the mode solution. The near-field contribution of the  $n = \pm 3$  components is confirmed by the better phase match against the full Helmholtz solver prediction when it is accounted for. It is noted that the slight phase mismatch between the low-order network model and Helmholtz solvers, are associated with mean flow effects across the flames – a more detailed discussion on this is provided in Appendix (C).

#### 5.4. Non-linear flame model: slanted mode

The low-order network model has been shown able to accurately predict longitudinal, circumferential spinning and circumferential standing limit cycles when a nonlinear flame model is used. We now demonstrate that the more complicated slanted mode can also be captured. When the initial guess of the modal amplitude vector,  $\lambda$ , contains  $\lambda^{(0)}, \lambda^{(+1)}$  and  $\lambda^{(-1)}$  all with the same order of magnitude, a limit cycle solution in which the strengths of all the three of these modal components is the same order of magnitude is found. The amplitudes of all higher order modes are much smaller. This is a slanted mode limit cycle solution.

The predicted evolution of these modes with growth rate is shown in Fig. 11, along with comparison to Helmholtz solver results. There is good agreement for both the frequency and strengths of the modal components between the low-order network model predictions and the Helmholtz solver predictions. The frequency of the limit cycle is 481 Hz, slightly different to the longitudinal (480 Hz), spinning (492 Hz), and standing (492 Hz) limit cycle solutions.

It is further found that the  $\lambda^{(\pm 1)}$  components always have the same amplitudes, meaning that they give a standing wave, so the final solution is a combination of a standing wave and a purely longitudinal wave with the same frequency. This mode pattern has been experimentally identified by Bourguin et al. [7] but has not previously been accurately predicted by low-order modelling tools. It is known as a “slanted mode” because the velocity perturbation amplitudes over the 16 burner outlets exhibit a slanted pattern – one side of the 16 burners sees much larger amplitudes than the other side, with only one minimum and one maximum over the circumference. As shown in Fig. 12, the velocity perturbation amplitude exhibits a maximum at the 9<sup>th</sup> burner, gradually decreasing as we around to a minimum at

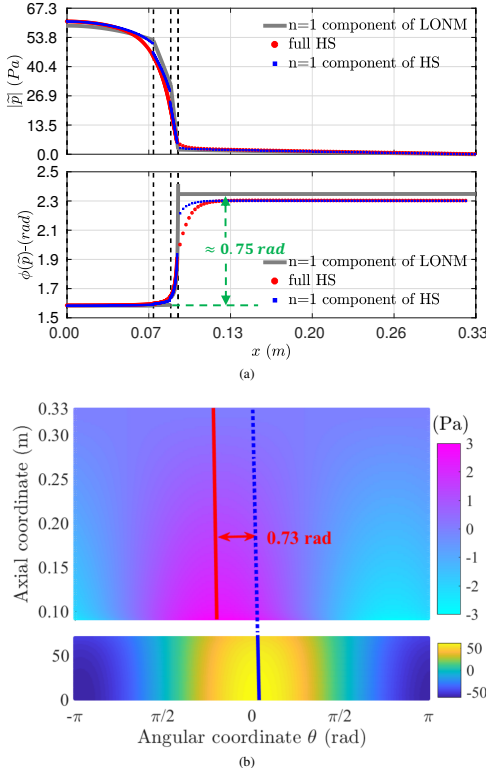


Figure 9: (Color online) Spinning limit cycle pressure distribution. (a) Axial variation of the amplitude and phase of the mode shape (at  $\theta = 0$ ), with only the  $n = 1$  component plotted for the low-order network model. (b) Helmholtz solver instantaneous snapshot prediction at an arbitrary time  $t = t_0$ , obtained from  $\text{Real}[\tilde{p}^{(1)}e^{i(\theta+\omega_0 t)}]$ .

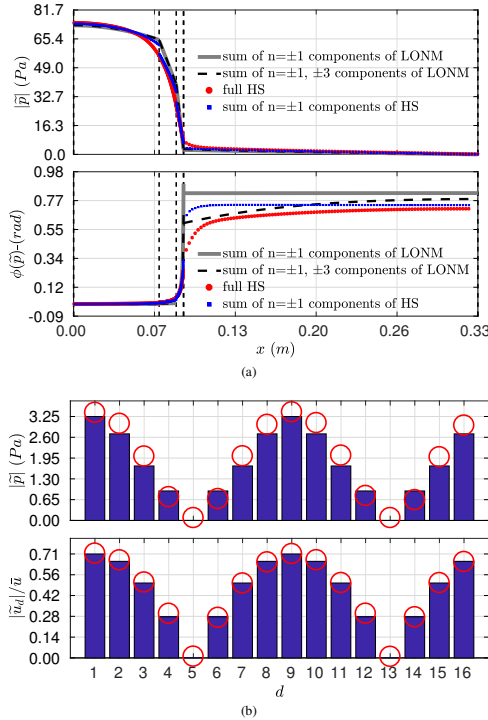


Figure 10: (Color online) Standing limit cycle perturbation distribution. (a) Axial variation of the amplitude and phase of the pressure mode shape at  $\theta = 0$  with “1st standing” denoting the combination of the  $n = \pm 1$  components and “1st + 3rd standing” denoting the combination of the  $n = \pm 1, \pm 3$  components; (b) pressure and velocity perturbations at each of the 16 burner outlets, with blue columns denoting the low-order network model and red circles the Helmholtz solver. The central axis of the  $d^{\text{th}}$  burner is at  $\Psi_d = 2\pi(d - 1)/16$ .

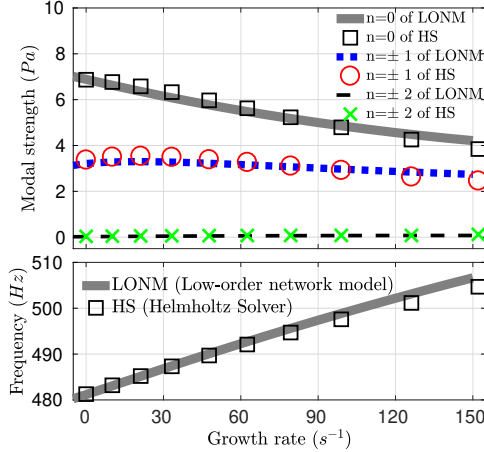


Figure 11: (Color online) Evolution of the slanted mode. (Top) The strength of different modal components in  $\lambda$  at the plenum inlet; (Bottom) the mode frequency.  $N = 5$  is used in the low-order network model, but only  $|n| \leq 2$  is plotted for the strengths. The Helmholtz solver results are obtained with  $\varepsilon = 17 s^{-1}$ .

the 1<sup>st</sup> burner. These predictions are in agreement with those from the 3-D Helmholtz solver and in agreement with experimental findings [7]. It is interesting to note that the pressure amplitude sees a maximum near the 1<sup>st</sup> burner and a minimum at the 9<sup>th</sup>, being anti-correlated to the velocity amplitude. This implies that the axial acoustic impedances differ across the burner outlets, and are dependent on azimuth angle.

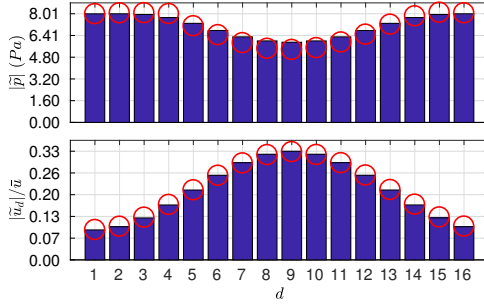


Figure 12: (Color online) (Top) Pressure and (Bottom) velocity perturbation amplitudes at each of the 16 burner outlets for the slanted limit cycle. Blue columns denote the low-order network model and red circles the Helmholtz solver. The central axis of the  $d^{\text{th}}$  burner is at  $\Psi_d = 2\pi(d - 1)/16$ .

The slanted mode is now analysed in more detail. Figure 13 shows the spatial variation, with both azimuth angle and axial distance, of the pressure modeshape as predicted by the Helmholtz solver. This is done for the full Helmholtz

solver solution, and for its  $n = 0$  and  $n = \pm 1$  components. The  $n = 0$  longitudinal and  $n = \pm 1$  standing components exhibit the same order of magnitude. Their strengths greatly exceed those of higher order components, as shown in Fig. 14a where the summation of the longitudinal and standing components, from both the low-order network model and the Helmholtz solver, recover the original mode shape almost perfectly. Figure 14(a) also confirms that the low-order network model accurately captures the modal coupling and the two-dimensional propagating characteristics of the slanted mode. A more detailed discussion on solution convergence and higher order modal couplings across the flames can be found in Appendix (B).

Figure 14 also compares the axial variation of the longitudinal and standing modal components between the low-order network model and the Helmholtz solver. Very good match in both amplitude and phase is achieved, confirming that the mode shapes for each modal component are accurately captured in detail. Note that the small phase difference for the standing component in Fig. 14(c) is mainly due to the mean flow effect across the flames, as discussed in Appendix (C).

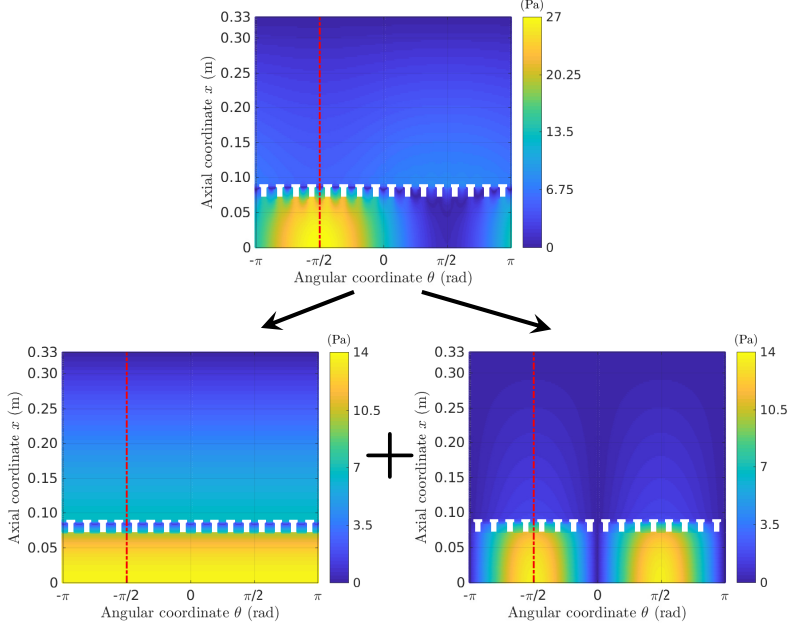


Figure 13: (Color online) Helmholtz solver results. (Top) the pressure mode shape,  $|\tilde{p}(x, \theta)|$ , of the slanted limit cycle; (bottom left) its longitudinal,  $|\tilde{p}^{(0)}(x)|$ , and (bottom right) its combined  $n = \pm 1$  components,  $|\tilde{p}^{(1)}(x)e^{i\theta} + \tilde{p}^{(-1)}(x)e^{-i\theta}|$ .

## 6. Effect of the initial guess on the limit cycle solution

It should be noted that all of the limit cycle solutions discussed in Section 5 were obtained for the same combustor – the same geometry, mean flow and nonlinear flame model. The only difference leading to the different predicted

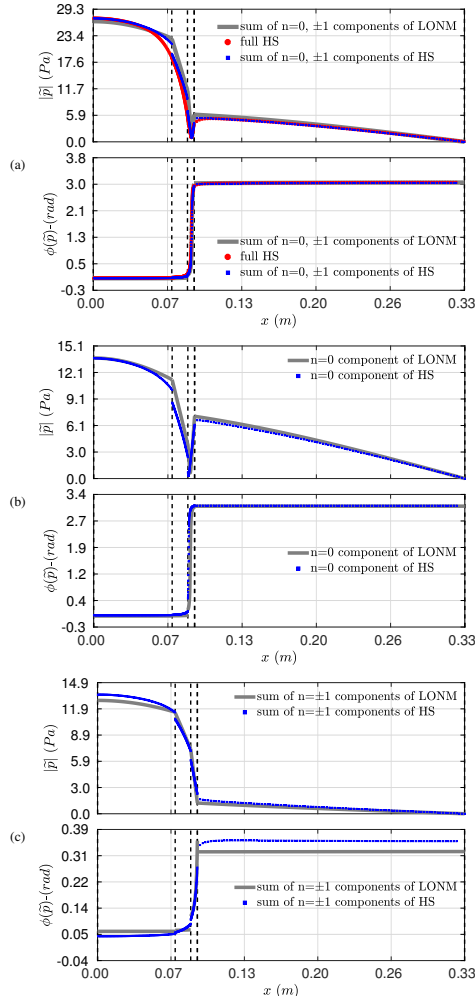


Figure 14: (Color online) Axial variation of the pressure mode shape for the slanted limit cycle at  $\theta = -\pi/2$  (the red dash line in Fig. 13). (a) Overall pressure, with “full HS” denoting the original Helmholtz solver result, and “sum of  $n = 0, \pm 1$  components of LONM” and “sum of  $n = 0, \pm 1$  components of HS” the sum of the longitudinal and first standing modal components, (b) only the longitudinal and (c) only the first standing modal components.

limit cycles was that of the initial guess used at the start of the eigenvalue problem in Eq. (22).

The link between the initial guess and the final limit cycle solution is now investigated. As we are only interested in the final limit cycle solution, the growth rate is forced to zero to always yield limit cycle solutions. Figure 15 shows how, for a given frequency guess, the final limit cycle solution varies with the modal amplitudes of the initial guess of  $\lambda$ . The top plot shows that by starting sufficiently close to a spinning solution (either  $n = 1$  or  $n = -1$ ), the final limit cycle will be that spinning mode, while if the initial guess sets the two components ( $n = \pm 1$ ) to the same order, the limit cycle solution will be the standing mode. When a non-zero longitudinal component is included together with both of the  $n = \pm 1$  components (assumed to have the same strengths), Fig. 15 (Bottom) shows that the limit cycle solutions can be the longitudinal, standing, or the slanted mode, depending on which solution is the initial guess close to.

It is clear that longitudinal, spinning, standing, and slanted modes are all limit cycle solutions of the present annular combustion system. This indicates that one or more may appear in reality or in full time domain simulations. The choice of which one(s) appear will depend on environmental noise, initial conditions and the stabilities of these limit cycle solutions. For the slanted mode, the stability of limit cycle solutions has yet to be systematically studied [18, 27]. Full time domain analysis may help to clarify this.

## 7. Standing-slanted-longitudinal mode switches

For all previous cases with a nonlinear flame model, the model in Eqs. (23) and (24) was used, with a flame time delay,  $\tau_f^L = 1$  ms. A slanted limit cycle was found at ( $f = 481.16$  Hz,  $|\lambda^{(0)}| = 6.89$  Pa,  $|\lambda^{(1)}| = |\lambda^{(-1)}| = 3.21$  Pa). By defining the ratio between the strengths of the standing and longitudinal modal components as  $\lambda_S/\lambda_L = (|\lambda^{(1)}| + |\lambda^{(-1)}|)/|\lambda^{(0)}|$ , we find that  $\lambda_S/\lambda_L = 0.93$  for the slanted mode in Section 5.4, shown by the green star in Fig. 16.

If we now very slightly increase the flame time delay from  $\tau_f^L = 1$  ms to  $\tau_f^L = 1.01$  ms (with all other system parameters unchanged),  $\lambda_S/\lambda_L$  is seen to decrease dramatically, becoming zero when  $\tau_f^L > 1.01$  ms, as shown in Fig. 16. This means that the slanted mode has switched to a purely longitudinal mode, for an increase in flame time delay of just 0.01 ms. If we slightly decrease  $\tau_f^L$  from 1 ms,  $\lambda_S/\lambda_L$  is firstly seen to increase gradually from 0.93 to about 3.3 at  $\tau_f^L \approx 0.85$  ms, but then increase dramatically to nearly infinity at  $\tau_f^L \approx 0.81$  ms. It remains a pure standing mode for  $\tau_f^L < 0.81$  ms. The frequency of the slanted mode increases significantly from 481.16 Hz to around 605 Hz for the time delay decreasing from 1 ms to 0.81 ms. These mode switches have been checked to be both converged with modal expansion truncation number  $N$  and to be consistent with the 3-D Helmholtz solver predictions.

The very strong sensitivity to flame model time delay of the ratio between the standing and longitudinal modal components indicates that accurately predicting the mode pattern may need very accurate determination of the flame response. Furthermore, predicting limit cycle characteristics requires the acoustic energy balance between input from the unsteady flames and dissipation to be accurately captured. Due to their different mode shapes, acoustic dissipation in a given system will typically differ between longitudinal and standing modal components. This indicates the importance of correctly capturing the standing to longitudinal ratio for studying the slanted mode.

## 8. Conclusion

A systematic investigation into nonlinear modal couplings in annular combustors has been performed using a 2-D low-order network model framework and a 3-D Helmholtz solver, both incorporating the same nonlinear flame model. By carefully comparing predictions for a representative simplified annular combustor geometry incorporating simple nonlinear flame models, detailed quantitative evidence is provided to show that the modal expansion based low-order network model approach can accurately predict limit cycle solutions with different mode patterns. This includes purely longitudinal, circumferentially spinning, circumferentially standing, and even the more complicated slanted modes. For the first time, nonlinear couplings both between circumferentially counter-rotating modal components and between circumferential and longitudinal modal components are captured using the low-order network modelling framework and are validated against Helmholtz solver predictions. It is shown that limit cycle solutions with very different spatial mode patterns may all exist in a given thermoacoustic system. Furthermore, switches between standing, slanted and longitudinal modes can occur when system parameters, such as the flame model time delay, undergo slight changes. The present low-order network model takes negligible computational time. It has the advantages of

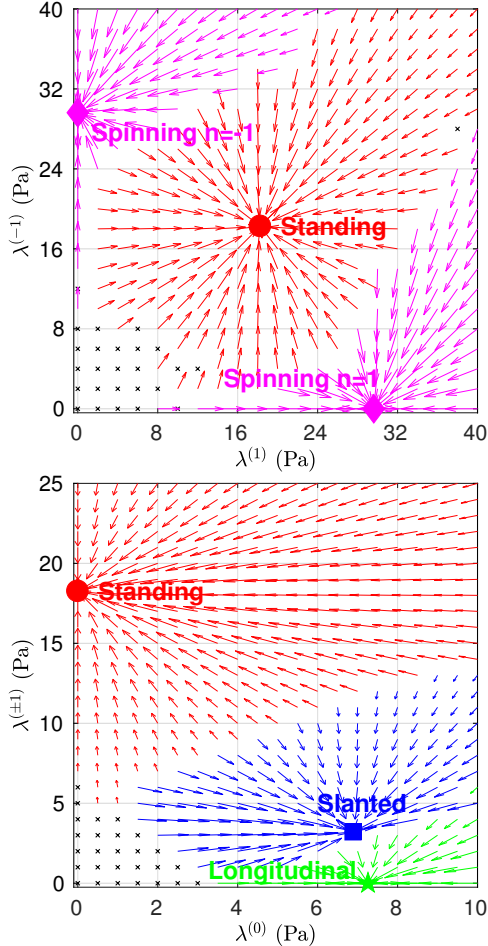


Figure 15: (Color online) Dependence of limit cycle mode solutions with modal amplitudes in the initial guess. (Top) only  $\lambda^{(1)}$  and  $\lambda^{(-1)}$  are non-zero, and (Bottom) only  $\lambda^{(\pm 1)}$  (both the same) and  $\lambda^{(0)}$  are non-zero in the initial guess for  $\lambda$ .  $N = 5$  and the initial frequency guess is  $f_{guess} = 485 \text{ Hz}$ . The arrows and colors denote the solution found from each initial guess, and the black cross means no solution was found – the solver converges to a local minimum instead of a solution.

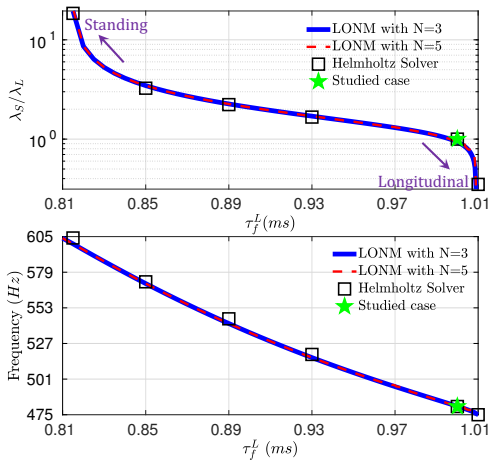


Figure 16: (Color online) The effect of varying the flame time-delay,  $\tau_f^L$ , on mode switches from slanted to standing or longitudinal. (Top) The ratio between the strengths of the standing and longitudinal modal components and (Bottom) the frequency.  $N$  is the modal expansion truncation number. In the Helmholtz solver calculations the damping coefficients  $\varepsilon$  ranges from a value of  $\varepsilon=11.5$  to  $30\text{ s}^{-1}$  for the standing and longitudinal modes, respectively.

allowing for generic acoustic boundary conditions at either end of the system and accounting for mean flow effects such as acoustic damping at flow expansions, entropy and vorticity waves. It is therefore less restrictive than many recent low-order modelling approaches for annular combustors.

## 9. Acknowledgements

The authors would like to gratefully acknowledge the Engineering and Physical Sciences Research Council (EPSRC) grant (code EP/P003036/1) CHAMBER (2017-2019) and the ERC Starting Grant (No: 305410 ACOULO-MODE (2013-2018) for supporting the current research.

# Appendices

## A. Transfer Matrices

The wave-to-flow and flow-to-flux transfer matrices with circumferential wavenumber  $n$  for an annular duct (the plenum or the combustor) are

$$\mathbf{M}_{\mathbf{W2F}}^{(n)} = \begin{pmatrix} 1 & 1 & 0 & 0 \\ \frac{1}{\tilde{c}^2} & \frac{1}{\tilde{c}^2} & -\frac{1}{\tilde{c}^2} & 0 \\ -\frac{1}{\tilde{c}^2 n^+} & \frac{\tilde{c}^2}{\tilde{c}^2 n^-} & 0 & \frac{n}{\tilde{p} c} \\ \frac{\tilde{p} \tilde{a}^{n+}}{\tilde{p} \tilde{a}^{n-}} & \frac{\tilde{p} \tilde{a}^{n-}}{\tilde{p} \tilde{a}^{n+}} & 0 & -\frac{k_0 R}{\tilde{p} c} \end{pmatrix}, \quad (\text{A.1})$$

$$\mathbf{M}_{\mathbf{F2J}}^{(n)} = S \begin{pmatrix} 0 & \bar{u} & \bar{p} & 0 \\ 1 & \bar{u}^2 & 2\bar{p}\bar{u} & 0 \\ 0 & 0 & 0 & \bar{R}\bar{p}\bar{u} \\ \frac{\gamma\bar{u}}{\gamma-1} & \frac{\bar{u}^3}{2} & \left(\frac{\gamma\bar{p}}{\gamma-1} + \frac{3\bar{p}\bar{u}^2}{2}\right) & 0 \end{pmatrix}. \quad (\text{A.2})$$

The wave-to-flow and flow-to-flux transfer matrices for plane waves at each of the premix duct inlet are

$$\mathbf{M}_{\mathbf{W2F}}^{(p)} = \begin{pmatrix} 1 & 1 & 0 \\ \frac{1}{\tilde{c}^2} & \frac{1}{\tilde{c}^2} & -\frac{1}{\tilde{c}^2} \\ \frac{1}{\tilde{p} c} & \frac{-1}{\tilde{p} c} & 0 \end{pmatrix}, \quad (\text{A.3})$$

$$\mathbf{M}_{\mathbf{F2J}}^{(p,2^+)} = S \begin{pmatrix} 0 & \bar{u} & \bar{p} \\ \frac{C_v}{\tilde{S}\bar{p}} & \frac{-\gamma C_v}{\tilde{S}\bar{p}} & 0 \\ \frac{\gamma\bar{u}}{\gamma-1} & \frac{\bar{u}^3}{2} & \left(\frac{\gamma\bar{p}}{\gamma-1} + \frac{3\bar{p}\bar{u}^2}{2}\right) \end{pmatrix}, \quad (\text{A.4})$$

where  $C_v$  is the heat capacity at constant volume. The flow-to-flux transfer matrices for plane waves at each of the premix duct outlet is

$$\mathbf{M}_{\mathbf{F2J}}^{(p,3^-)} = S_2 \begin{pmatrix} 0 & \bar{u} & \bar{p} \\ \frac{S_3}{S_2} & \bar{u}^2 & 2\bar{p}\bar{u} \\ \frac{\gamma\bar{u}}{\gamma-1} & \frac{\bar{u}^3}{2} & \left(\frac{\gamma\bar{p}}{\gamma-1} + \frac{3\bar{p}\bar{u}^2}{2}\right) \end{pmatrix}. \quad (\text{A.5})$$

## B. Solution convergence and modal couplings across the flames

Convergence of the limit cycle solutions of the longitudinal, spinning, standing, and slanted modes with increasing modal expansion truncation number,  $N$ , are shown in Fig. B.1. It can be seen that  $N = 1$  gives converged results for both the longitudinal and spinning modes. This is because these two modes are both modally uncoupled – the longitudinal mode involves only the  $n = 0$  modal component and the spinning mode only the  $n = 1$  modal component. This is further confirmed by the Fourier amplitudes of different modal components of the pressure and velocity perturbations

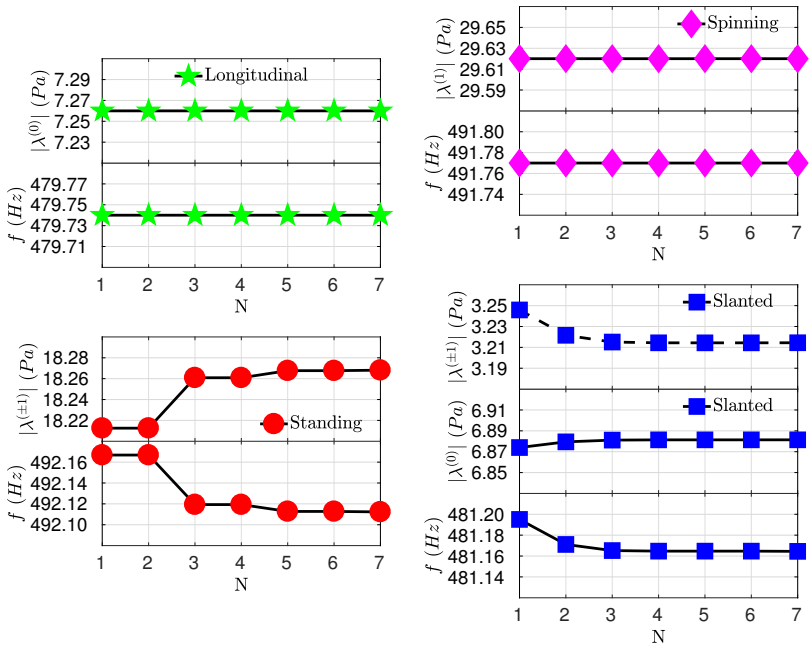


Figure B.1: (Color online) Convergence of the limit cycle solutions in Section 5 with modal truncation number,  $N$ . Both the strengths of the dominant modal components and the frequency are shown for each of these modes.

just ahead and after the flames, and the flame heat release oscillations in Fig. B.2 where it is seen that  $n' = 0$  is the only non-zero component for the longitudinal mode and  $n' = 1$  the only non-zero component for the spinning mode. For the standing mode limit cycle, even though the mode is dominated by the  $n = \pm 1$  components and the mode solution with  $N = 1$  generally gives accurate enough results, increasing  $N$  from 1 to 5 gives further slight improvements in the mode solution. This is because the nonlinear flame model couples the dominant  $n = \pm 1$  components with higher order modal components to generate higher order perturbations near the flames, as shown in Fig. B.3a. These are evanescent waves which decay exponentially away from the flames, hence they have little effect on the mode solutions for the cases considered in the present paper. Similar effect can also be seen in Fig. B.1 and Fig. B.3b for the slanted mode. Note that more general couplings involving more modal components may exist when higher frequency modes are considered, or when the combustion system becomes shorter and higher order evanescent waves become more important.

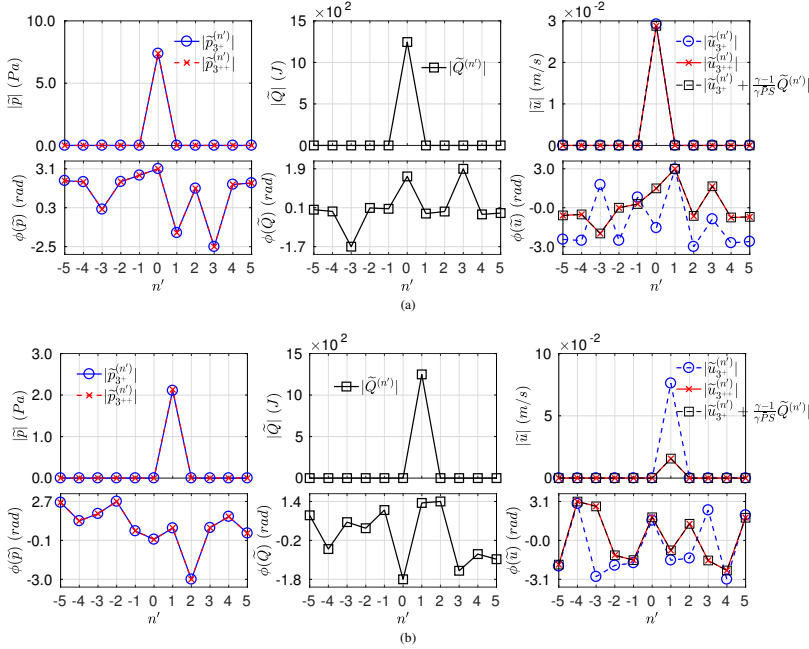


Figure B.2: (Color online) (Left) Pressure, (Middle) heat release rate, and (right) velocity perturbations just before and after the flames for different modal components during different limit cycles in Section 5 – (a) the longitudinal mode, (b) the spinning mode.  $\tilde{p}^{(n')}$ ,  $\tilde{Q}^{(n')}$ , and  $\tilde{u}^{(n')}$  are the Fourier amplitudes of the modal component with circumferential wave number  $n'$  for pressure, heat release, and velocity perturbations respectively. Subscripts  $_{3+}$  and  $_{3++}$  denote axial locations just before and after the flames respectively – as shown by  $x_3^\pm$  and  $x_3^{\pm\pm}$  in Fig. 2.

Modal couplings across the flames are now considered. As the mean flow Mach number just ahead of the flame is

very small,  $O(10^{-3})$ , jump conditions across the flames, Eq. (18), can be simplified to give

$$\bar{P}_{3^+}^{(n')} \approx \bar{P}_{3++}^{(n')}, \quad (\text{B.1a})$$

$$\bar{n}_{3^+}^{(n')} + \frac{\gamma - 1}{\gamma \bar{p} S} \bar{Q}^{(n')} \approx \bar{n}_{3++}^{(n')}, \quad (\text{B.1b})$$

where  $\bar{p}$  and  $S$  are the mean pressure and cross-sectional area. The Fourier amplitude of the  $n'$ th modal component of the heat release rate perturbation is

$$\bar{Q}^{(n')} = \sum_{d=1}^D \bar{Q}_d e^{-in' \Phi_d}. \quad (\text{B.2})$$

Equation (B.1) show that in the absence of heat release rate oscillations, each modal component of pressure and velocity is continuous across the flames – no modal coupling occurs. If the flame model is linear, substituting the velocity perturbations and flame model into Eq. (B.2) (note that  $D \gg n'$ ) shows that  $\bar{Q}^{(n')}$  is only related to the  $n'$ th modal component of the velocity perturbation just before the flame,  $\bar{v}_{3^+}^{(n')}$  – no modal coupling occurs. However, when a nonlinear flame model is considered,  $\bar{Q}^{(n')}$  involves velocity perturbations with different  $n'$ s – different modal components are coupled. The perturbation relations for each modal component across the flames are shown in Figs. B.2 and B.3 for all the four limit cycle modes in Section 5. Several conclusions can be drawn: firstly, the widely used flame jump condition [40] is satisfied for each modal component in annular combustors, as given here by Eq. (B.1). Secondly, the flame nonlinearity is the source of modal couplings. Thirdly, with nonlinear flame models, longitudinal and spinning modes both involve only one modal component so are uncoupled solutions, but standing and slanted modes involve more modal components which are coupled by the flames.

### C. The effect of the mean flow across the flames on the axial mode shape of the standing mode

In Fig. 10a, a slight but noticeable phase difference between the low-order network and Helmholtz solver predictions is observed, for both the first standing component and the original mode shape. We now show that these differences are mainly due to the small mean flow effect across the flames. Figure C.1 shows that when the mean flow speeds just before and after the flames ( $x_3^+$  and  $x_3^{++}$  in Fig. 2) are artificially enforced to tend to zero (the flames' heat release rates and the mean flow everywhere else are assumed unaffected), the predicted pressure phases agree much better with the Helmholtz solver, for both the 1st standing component and the original mode shape.

### References

- [1] S. M. Correa, Power generation and aeropropulsion gas turbines: from combustion science to combustion technology, Symposium (International) on Combustion 27 (1998), volume 27, Elsevier, 1793–1807.
- [2] A. P. Dowling, S. R. Stow, Acoustic analysis of gas turbine combustors, Journal of Propulsion and Power 19 (2003) 751–764.
- [3] J. O'Connor, V. Acharya, T. Lieuwen, Transverse combustion instabilities: Acoustic, fluid mechanic, and flame processes, Progress in Energy and Combustion Science 49 (2015) 1–39.
- [4] T. Poinsot, Prediction and control of combustion instabilities in real engines, Proceedings of the Combustion Institute 36 (2017) 1–28.
- [5] W. Krebs, P. Flohr, B. Prade, S. Hoffmann, Thermoacoustic stability chart for high-intensity gas turbine combustion systems, Combustion Science and Technology 174 (2002) 99–128.
- [6] N. A. Worth, J. R. Dawson, Modal dynamics of self-excited azimuthal instabilities in an annular combustion chamber, Combustion and Flame (2013).
- [7] J.-F. Bourgoin, D. Durox, J. P. Moeck, T. Schuller, S. Candel, A new pattern of instability observed in an annular combustor: The slanted mode, Proceedings of the Combustion Institute 35 (2015) 3237–3244.
- [8] N. A. Worth, J. R. Dawson, Effect of equivalence ratio on the modal dynamics of azimuthal combustion instabilities, Proceedings of the Combustion Institute 36 (2017) 3743–3751.
- [9] K. Prieur, D. Durox, T. Schuller, S. Candel, A hysteresis phenomenon leading to spinning or standing azimuthal instabilities in an annular combustor, Combustion and Flame 175 (2017) 283–291.
- [10] M. Bauerheim, F. Nicoud, T. Poinsot, Progress in analytical methods to predict and control azimuthal combustion instability modes in annular chambers, Physics of Fluids 28 (2016) 21303.
- [11] G. Staffelbach, L. Y. M. Gicquel, G. Boudier, T. Poinsot, Large eddy simulation of self excited azimuthal modes in annular combustors, Proceedings of the Combustion Institute 32 (2009) 2909–2916.
- [12] P. Wolf, G. Staffelbach, L. Y. M. Gicquel, J.-D. Müller, T. Poinsot, Acoustic and large eddy simulation studies of azimuthal modes in annular combustion chambers, Combustion and Flame 159 (2012) 3398–3413.

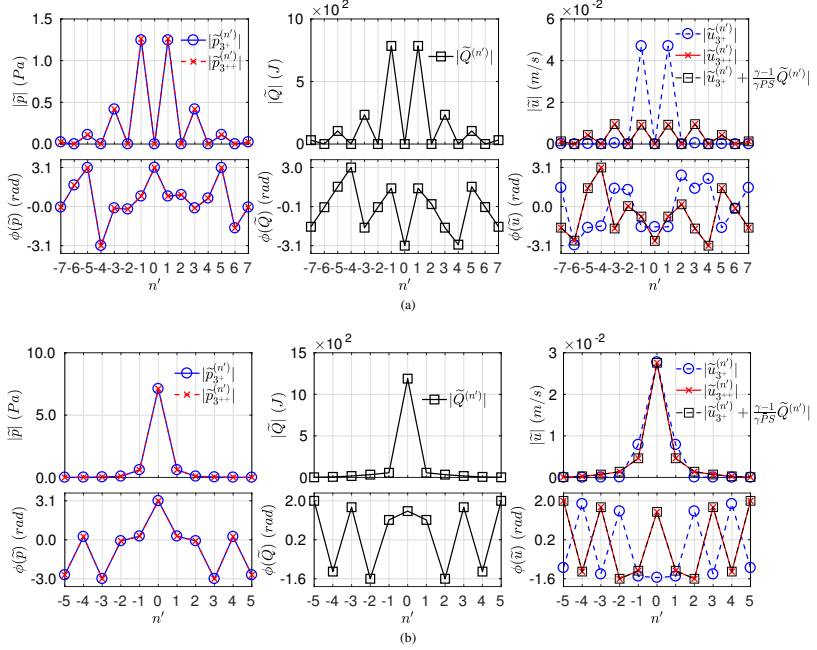


Figure B.3: (Color online) (Left) Pressure, (Middle) heat release, and (right) velocity perturbations just before and after the flames for different modal components during different limit cycles in Section 5 – (a) the standing mode, (b) the slanted mode.  $\tilde{p}^{(n')}$ ,  $\tilde{Q}^{(n')}$ , and  $\tilde{u}^{(n')}$  are the Fourier amplitudes of the modal component with circumferential wave number  $n'$  for pressure, heat release, and velocity perturbations respectively.

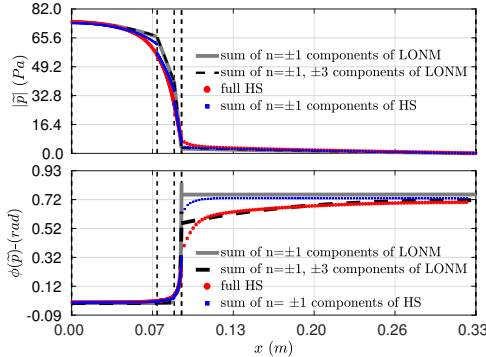


Figure C.1: (Color online) The axial mode shape of the standing limit cycle with  $\tilde{u} \rightarrow 0$  across the flames (at  $x_3^+$  and  $x_3^{++}$  in Fig. 2 where flow perturbations just before and after the flames are calculated).

- [13] M. Bauerheim, J.-F. Parmentier, P. Salas, F. Nicoud, T. Poinsot, An analytical model for azimuthal thermoacoustic modes in an annular chamber fed by an annular plenum, *Combustion and Flame* 161 (2014) 1374–1389.
- [14] M. Bauerheim, P. Salas, F. Nicoud, T. Poinsot, Symmetry breaking of azimuthal thermo-acoustic modes in annular cavities : a theoretical study, *Journal of Fluid Mechanics* 760 (2014) 431–465.
- [15] M. Bauerheim, M. Cazalens, T. Poinsot, A theoretical study of mean azimuthal flow and asymmetry effects on thermo-acoustic modes in annular combustors, *Proceedings of the Combustion Institute* 35 (2015) 3219–3227.
- [16] N. Noiray, M. Bothien, B. Schuermans, Investigation of azimuthal staging concepts in annular gas turbines, *Combustion Theory and Modelling* 15 (2011) 585–606.
- [17] G. Ghirardo, M. P. Juniper, Azimuthal instabilities in annular combustors: standing and spinning modes, *Proceedings of the Royal Society A: Mathematical, Physical and Engineering Sciences* 469 (2013) 20130232–20130232.
- [18] G. Ghirardo, M. P. Juniper, J. P. Moeck, Weakly nonlinear analysis of thermoacoustic instabilities in annular combustors, *Journal of Fluid Mechanics* 805 (2016) 52–87.
- [19] C. Li, D. Yang, S. Li, M. Zhu, An analytical study of the effect of flame response to simultaneous axial and transverse perturbations on azimuthal thermoacoustic modes in annular combustors, *Proceedings of the Combustion Institute* 37 (2019) 5279–5287.
- [20] S. R. Stow, A. P. Dowling, A time-domain network model for nonlinear thermoacoustic oscillations, *Journal of Engineering for Gas Turbines and Power* 131 (2009).
- [21] A. S. Morgans, S. R. Stow, Model-based control of combustion instabilities in annular combustors, *Combustion and Flame* 150 (2007) 380–399.
- [22] S. R. Stow, A. P. Dowling, Thermoacoustic oscillations in an annular combustor, *Proceedings of ASME Turbo Expo* 200 (2001).
- [23] S. Evesque, W. Polifke, Low-order acoustic modelling for annular combustors: Validation and inclusion of modal coupling, *Proceedings of ASME Turbo Expo* (2002), American Society of Mechanical Engineers, 321–331.
- [24] S. Evesque, W. Polifke, C. Pankiewitz, Spinning and azimuthally standing acoustic modes in annular combustors, 9th AIAA/CEAS Aeroacoustics Conference (2003).
- [25] S. R. Stow, A. P. Dowling, Low-order modelling of thermoacoustic limit cycles, *Proceedings of ASME Turbo Expo* (2004) GT2004–5425.
- [26] D. Yang, A. S. Morgans, Low-order network modeling for annular combustors exhibiting longitudinal and circumferential modes, *Proceedings of ASME Turbo Expo* (2018) GT2018–76506.
- [27] A. Orchini, G. A. Mensah, J. P. Moeck, Effects of nonlinear modal interactions on the thermoacoustic stability of annular combustors, *Journal of Engineering for Gas Turbines and Power* (2018).
- [28] B.-T. Chu, L. S. G. Kovászny, Non-linear interactions in a viscous heat-conducting compressible gas, *Journal of Fluid Mechanics* 3 (1958) 494–514.
- [29] J. Li, A. S. Morgans, Time domain simulations of nonlinear thermoacoustic behaviour in a simple combustor using a wave-based approach, *Journal of Sound and Vibration* 346 (2015) 345–360.
- [30] D. Yang, A. S. Morgans, Acoustic Models for Cooled Helmholtz Resonators, *AIAA Journal* 55 (2017) 3120–3127.
- [31] B. S. Massey, A. J. Ward-Smith, *Mechanics of fluids*, S. Thorne, 1998.
- [32] Y. Méry, Impact of heat release global fluctuations and flame motion on transverse acoustic wave stability, *Proceedings of the Combustion Institute* 36 (2017) 3889–3898.
- [33] S. R. Stow, A. P. Dowling, T. P. Hynes, Reflection of circumferential modes in a choked nozzle, *Journal of Fluid Mechanics* 467 (2002) 215–239.

- [34] D. Laera, T. Schuller, K. Prieur, D. Durox, S. M. Camporeale, S. Candel, Flame describing function analysis of spinning and standing modes in an annular combustor and comparison with experiments, *Combustion and Flame* 184 (2017) 136–152.
- [35] D. Laera, K. Prieur, D. Durox, T. Schuller, S. M. Camporeale, S. Candel, Impact of Heat Release Distribution on the Spinning Modes of an Annular Combustor With Multiple Matrix Burners, *Journal of Engineering for Gas Turbines and Power* 139 (2017) 051505.
- [36] D. Yang, A. S. Morgans, The acoustics of short circular holes opening to confined and unconfined spaces, *Journal of Sound and Vibration* 393 (2017) 41–61.
- [37] M. C. A. M. Peters, A. Hirschberg, A. J. Reijnen, A. P. J. Wijnands, Damping and reflection coefficient measurements for an open pipe at low Mach and low Helmholtz numbers, *Journal of Fluid Mechanics* 256 (1993) 499–534.
- [38] A. P. Dowling, Nonlinear self-excited oscillations of a ducted flame, *Journal of Fluid Mechanics* 346 (1997) 271–290.
- [39] J.-F. Bourgouin, D. Durox, J. P. Moeck, T. Schuller, S. Candel, Characterization and Modeling of a Spinning Thermoacoustic Instability in an Annular Combustor Equipped With Multiple Matrix Injectors, *Journal of Engineering for Gas Turbines and Power* 137 (2014) 021503.
- [40] T. Poinsot, D. Veynante, *Theoretical and numerical combustion*, Edwards, 2005.